Ultrasound-responsive nanocarriers with siRNA and Fe_3O_4 regulate macrophage polarization and phagocytosis for augmented non-small cell lung cancer immunotherapy

Ming Li[1†], Yuanyuan Li[1†], Jun Zheng[2†], Zhen Ma[3], Jianye Zhang[4], Hao Wu[1], Yangyang Zhu[1], Pan Li[2*] and Fang Nie[1*]

Abstract

The immunosuppressive tumor microenvironment (TME) significantly inhibits the effective anti-tumor immune response, greatly affecting the efficacy of immunotherapy. Most tumor-associated macrophages (TAMs) belong to the M2 phenotype, which contributes significantly to the immunosuppressive effects in non-small cell lung cancer (NSCLC) TME. The interaction between signal regulatory protein α (SIRPα) expressed on macrophages and CD47, a transmembrane protein overexpressed on cancer cells, activates the "eat-me-not" signaling pathway, inhibiting phagocytosis. In this study, a folic acid (FA)-modified ultrasound responsive gene/drugs delivery system, named FA@ PFP @ Fe_3O_4 @LNB-SIRPα siRNA (FA-PFNB-SIRPα siRNA), was developed using 1,2-dioleoacyl-3-trimethylammonium-propane (DOTAP), FA-1,2-distearoyl-sn-glycero-3-phosphoethanolamine-N- [amino (polyethylene glycol)2000] (DSPE-PEG2000-FA), cholesterol, and perfluoropentane (PFP), for the delivery of siRNA encoding SIRPα mRNA and immune adjuvant Fe_3O_4 nanoparticles. Under ultrasound conditions, the nanobubbles effectively transfected macrophages, inhibiting SIRPα mRNA and protein expression, promoting the phagocytosis of TAMs, and synergistically reversing M2 polarization. This system promotes the infiltration of T cells, enhances the proliferation and activation of cytotoxic T cells, and inhibits the infiltration of immunosuppressive cells in tumor tissues. Administration of FA-PFNB-SIRPα siRNA combined with ultrasound significantly inhibits NSCLC progression. The study highlights the potential of ultrasound nanotechnology-enabled delivery of SIRPα siRNA and Fe_3O_4 as an effective strategy for macrophage-based immunotherapy to reshape the immunosuppressive TME for cancer therapy.

Keywords Ultrasound-responsive, Small interfering RNA (siRNA) delivery, Fe_3O_4 nanoparticles, CD47-SIRPα signaling, Non-small cell lung cancer (NSCLC)

[†]Ming Li, Yuanyuan Li and Jun Zheng have contributed equally to this work.
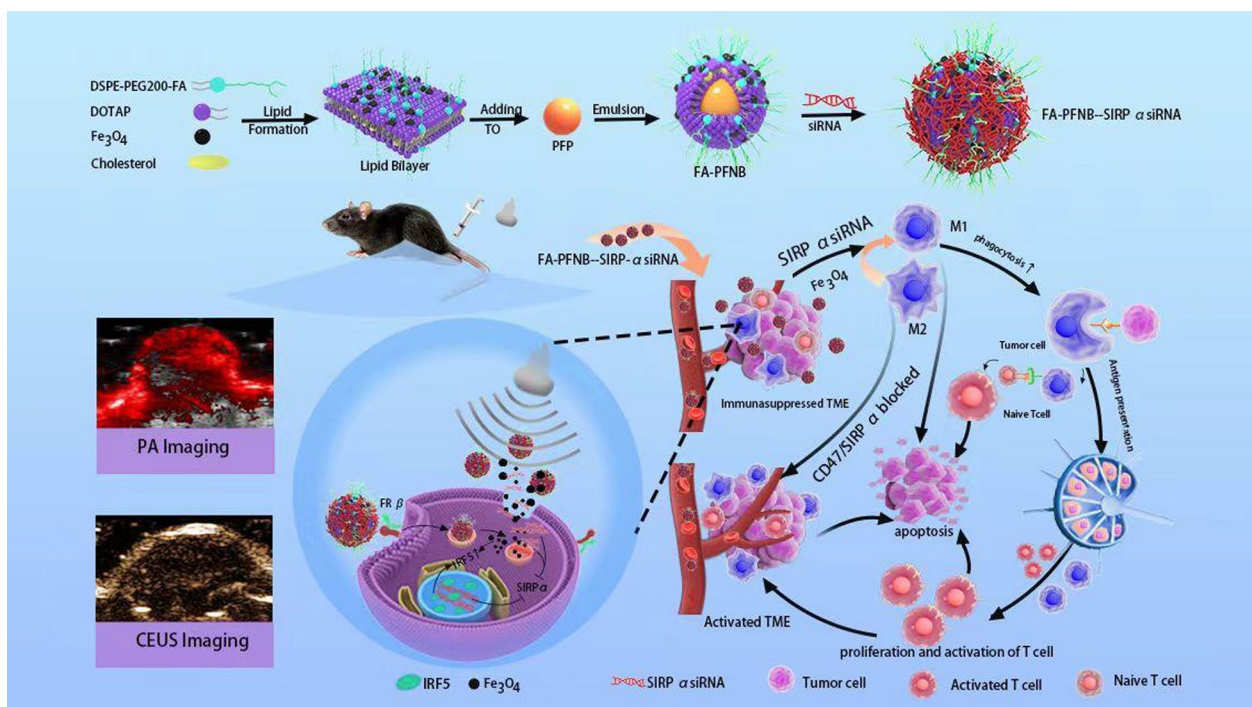
*Correspondence:
Pan Li
lipan@hospital.cqmu.edu.cn
Fang Nie
ery_nief@lzu.edu.cn
Full list of author information is available at the end of the article

Li *et al. Journal of Nanobiotechnology*   (2024) 22:605

Page 2 of 26

Graphical Abstract

Introduction

Non-small cell lung cancer (NSCLC) is the predominant form of lung cancer, with approximately 60% of patients being diagnosed at an advanced stage [1, 2]. At this point, the window for surgical resection closes, and the effectiveness of conventional chemotherapy and radiotherapy becomes limited [3]. In recent years, immunotherapy has shown promising outcomes in treating advanced lung cancer. However, only approximately 20% of patients with cancer experience a lasting response to immunotherapy, likely attributed to the diverse immune checkpoint variations, tumor microenvironment (TME) complexity, and other related factors. This significantly hampers the widespread adoption of immunotherapy [4]. Consequently, there is an urgent demand for discovering more efficient immunotherapy targets, and the potential breakthrough in NSCLC immunotherapy may depend on exploring combination therapies.

Studies indicate that tumor-associated macrophages (TAMs) are crucial in tumorigenesis, influencing treatment response and prognosis across various solid tumors [5]. TAMs comprise a diverse and dynamic population responsive to distinct local cues. They can undergo polarization into M1 or M2 types based on the signals within the TME [6]. M1-like TAMs can kill tumor cells by producing proinflammatory cytokines and recruiting T cells, while M2-like TAMs promote tumor cell growth and immune escape [7]. Reprogramming TAMs from M2-like to M1-like macrophages can effectively trigger anti-tumor immune responses and eliminate tumor-promoting effects [8]. Various anti-TAM strategies have been evaluated in preclinical studies and at different stages of clinical trials [6]. However, specifically manipulating TAMs to promote anti-tumor immune responses while preserving macrophages in healthy tissues remains a significant challenge.

Iron oxide (Fe_3O_4) nanoparticles have been found to induce the transition from M2-like to M1-like macrophages, making them a potential nanoplatform for cancer immunotherapy [9]. The high concentration of iron in TAMs may be involved in this reprogramming by activating the interferon-regulatory factor 5(IRF5) pathway to stimulate the inflammatory response [10]. However, the immune response induced by iron oxide nanoparticles alone is limited and cannot significantly inhibit tumor growth [11]. Tumor cells often upregulate the expression of CD47, and CD47 interacts with its signal regulatory protein α (SIRPα) on the surface of the macrophage [12]. This interaction provides a "self" signal that enables tumor cells to escape recognition and phagocytosis by

Li *et al. Journal of Nanobiotechnology*   (2024) 22:605

Page 3 of 26

macrophages, thus reducing antigen presentation capacity, inhibiting the activation of downstream T cells, and promoting tumor cell immune escape [13]. Blocking the CD47-SIRPα pathway can reactivate macrophages to phagocytose tumor cells, induce antigen-specific CD8^{+} T cell proliferation, and enhance innate and adaptive anti-tumor immune responses [14, 15]. Current clinical trials using monoclonal antibodies to block the CD47-SIRPα pathway have shown limited anticancer efficacy and systemic toxicity [16]. RNA interference (RNAi) is a highly effective gene-silencing technology widely used in gene therapy because of its specificity and low cost [17]. However, it is limited by low cellular uptake and easy nuclease-mediated degradation, thus requiring effective delivery vectors to protect siRNA entry into cells [18].

Nanoparticles (NPs) have emerged as promising gene delivery carriers, which can package and safeguard genes from enzymatic degradation, facilitate gene transport into the cytosol or elude lysosomal entrapment, and release gene cargo to the cellular translation apparatus [19]. While conventional nanoparticles offer numerous benefits, their practical use is hindered by ineffective tumor targeting and subpar gene transfection efficiency. Folic acid (FA) is a small molecular vitamin that boasts low molecular weight, no immune prototype, affordability, and ease of acquisition [20]. Moreover, it exhibits a strong affinity for receptors. In recent years, folic acid has been demonstrated to possess significant biological functions for the human body and can also serve as a targeting agent, particularly in cancer applications [21, 22]. Folic acid is used extensively in developing novel molecules, and various fields of research, including chemical, pharmaceutical, and biological research, require folic acid molecules [23, 24]. The folate receptor (FR), a cell surface glycoprotein with a high affinity for FA, facilitates the active uptake of FA [25]. FRβ is notably upregulated on M2-like macrophages, positioning FA as an effective modifier for targeted therapy of TAMs. This enhancement promotes nanoparticle accumulation in tumors while minimizing systemic toxicity [26].

Ultrasound-triggered drug release in nanoparticles offers a promising strategy to prevent premature drug release in non-targeted tissues and enhance drug penetration into tumor cells upon ultrasound (US) exposure [27]. Low-intensity focused ultrasound (LIFU) combined with nanomaterials elicits biological effects, including cavitation, mechanical impact, thermal effects, and acoustic pore formation. This approach is widely utilized in drug delivery and enhancing ultrasound imaging for tumor therapy [28]. The mechanical and thermal effects of LIFU can induce phase transition in liquid–gas materials like perfluoropentane (PFP), leading to acoustic droplet vaporization (ADV) and the generation of gas micro/

nanobubbles that enhance ultrasound imaging capabilities [29]. PFP, a biocompatible phase change material, can be encapsulated in liposome nanoparticles. Upon LIFU stimulation, PFP transitions to a gaseous state, forming micro/nanobubbles that amplify ultrasound imaging [30]. The continuous liquid-to-gas transition of PFP under persistent excitation, the sonoporation effect, and ultrasound-induced cavitation can boost targeted drug/gene delivery and enable personalized treatment approaches [31]. Therefore, incorporating Fe_3O_4 nanoparticles and SIRPα siRNA into nanobubbles can mitigate drug leakage and degradation, thus enhancing treatment efficacy.

This study introduces a TAMs-targeting siRNA/Fe_3O_4 ultrasonic-responsive delivery system engineered from FA-1,2-distearoyl-sn-glycero-3-phosphoethanolamine-N- [amino (polyethylene glycol)2000] (DSPE-PEG2000-FA), cholesterol,1,2-dioleoacyl-3-trimethylammonium-propane (DOTAP), Fe_3O_4 nanoparticles, and PFP to create a sophisticated nano complex, termed FA@PFP@Fe_3O_4@LNB(FA-PFNB). Nanobubbles (NBs) encapsulating Fe_3O_4 nanoparticles and SIRPα siRNA were then integrated to form the FA-PFNB-SIRPα siRNA complex. This study aims to investigate the potential of ultrasound and FA-modified non-viral vectors as an innovative strategy to enhance the delivery and efficacy of Fe_3O_4/SIRPα siRNA for treating NSCLC.

Materials and methods
Materials
DSPE-PEG2000, DSPE-PEG2000-FA, Cholesterol, and DOTAP were purchased from Ruixibio Co., Ltd. (Xi'an, China). Iron oxide nanoparticles with oleic acid (OA-Fe_3O_4) (Product Number: SOR10-02, 25 mg/mL, 5 nm) were purchased from Shanghai Sunr Biotech Co., Ltd (Shanghai, China), the preparation of Iron oxide nanoparticles by thermal decomposition method. Iron Oxide Nanoparticles in Chloroform have been coated with oleic acid for particle stability, and the oleic acid molecules' hydrophobic tail groups (hydrocarbon chains) line up to form a shell around the nanoparticle. PFP was purchased from Chongqing Zihai (Chongqing, China). Reagents such as trichloromethane ($CHCl_3$) and others of analytical grade were bought from Chongqing Chuandong Chemicals (Chongqing, China). Fetal bovine serum (FBS), Dulbecco's modified Eagle's Medium (DMEM), and Opti MEM were obtained from GIBCO BRL (Grand Island, USA). Agarose, Cell Counting Kit 8, 4′, 6-Diamidino-2-phenylindole (DAPI), trypsin, Annexin V-FITC/PI apoptosis detection kit, phosphate-buffered saline (PBS), and serum-free cell freezing medium were obtained from Biosharp (Anhui, China). Lipofectamine RNAiMAX Reagent and carboxyfluorescein succinimidyl ester (CFSE) were purchased from Thermo Fisher Scientific (Thermo

Li *et al. Journal of Nanobiotechnology*   (2024) 22:605

Page 4 of 26

Fisher, MA, USA). Recombinant Interleukin-4(IL-4) was purchased from PeproTech (USA). Trizol, primescript RT kit (036A), and SYBR Green PCR Master Mix were purchased from Takara (Shiga, Japan). DNase I, collagenase IV, hyaluronidase, and RBC lysis buffer were purchased from Solrabio (Beijing, China). The three double-stranded SIRPα siRNA and Cy5-NC siRNA used to knock down SIRPα gene expression in the study were obtained from Genepharma (Shanghai, China). The sequence of SIRPα siRNA is shown in Table S1. The flow cytometry antibodies used in this study are listed in Table S2, and the antibodies involved in the Western Blotting assay are shown in Table S3. Primers were obtained from ZerK-corp Biotech (Xi'an, China), and their specific sequences can be found in Table S4.

Screening of siRNA targeted SIRPα

To generate M2-like macrophages, RAW 264.7 cells were incubated in DMEM containing 20 ng/mL of IL-4 overnight. Specific siRNAs were designed to target SIRPα for silencing. Western blotting was performed to detect the effect of SIRPα gene silencing. Targeted siRNAs were transfected into M2-like macrophages using Lipofectamine RNAiMAX transfection reagent. M2-like macrophages were divided into four groups: the experimental group was transfected with siRNA targeting SIRPα (SIRPα-1, SIRPα-2, and SIRPα-3), and the control group was not transfected with siRNAs.

Synthesis of FA-PFNB-SIRPα siRNA

FA-PFNB was synthesized using a standard thin film hydration method [32]. Initially, DOTAP, cholesterol, and DSPE-PEG2000-FA were dissolved in 6 mL of trichloromethane in a round-bottom flask with a molar ratio of 3:1:1. Concurrently, OA-Fe_3O_4 nanoparticles were dissolved in $CHCl_3$ in a clear glass bottle and combined with the lipid solution at 25% of the lipid weight. The mixed solution was evaporated in a round-bottom flask using rotary evaporation to create a thin lipid film. Subsequently, 4 mL of PBS was introduced, and the solution was sonicated for 1 h at 60 °C. After adding 200 µL of PFP, the suspension was emulsified using a sonicator (Sonics and Materials Inc., USA) at 125 W power in an ice-water bath. Sonication was carried out for 8-min intervals of 5 s on and off. To remove excess reactants and free lipids, the emulsion was centrifuged at 8,000 rpm for 10 min at 4 °C, with this step repeated thrice for purification. The resulting vesicles were extruded through a 200-nm membrane and purified via dialysis.

To finalize the binding of siRNA to FA-PFNB (FA@ PFP@Fe_3O_4@LNBs), the positively charged FA-PFNB was merged with the siRNA solution in enzyme-free water and incubated at room temperature for 10 min.

The resulting prepared samples were denoted as FA-PFNB-siRNA. Within this designation, FA-PFNB-SIRPα siRNA identified combinations with SIRPα siRNA, while FA-PFNB-NC siRNA, serving as the control group, represented bindings with NC siRNA.

Characterization

Dynamic light scattering (DLS) (Nano-ZS, Malvern, UK) was used to detect Particle size and surface potential, including PFP@LNBs (PNB), PFP@Fe_3O_4 @LNBs-NC siRNA (PFNB-NC siRNA), PFP@LNBs-SIRP α siRNA (PNB-SIRPα siRNA), FA@ PFP@Fe_3O_4@LNBs (FA-PFNB), and FA@ PFP@Fe_3O_4 @LNBs-SIRPα siRNA (FA-PFNB-SIRPα siRNA). To evaluate the stability of FA-PFNB-SIRPα siRNA nanocarriers, the hydromechanical particle size of the nanocomposites was measured at 1, 3, 5, 7, and 10 days, respectively. Droplets of the diluted nanoparticle solution were added to the copper mesh and silicon wafer and dried at room temperature. The internal structure and morphology of FA-PFNB-SIRPα siRNA were obtained by Transmission electron microscope (TEM) (H-7600; Hitachi Ltd., Tokyo, Japan). The Fe concentration was analyzed with an atomic absorption spectrometer (Hitachi model Z-5000, Hitachi Ltd., Tokyo, Japan). The encapsulation efficiency and loading capacity of Fe_3O_4 were determined using the following equation:

$$\text{Encapsulation efficiency}(\%) = \text{mass of } \frac{Fe_3O_4}{\text{total}} Fe_3O_4 \times 100\%;$$

$$\text{Loading content (\%)} = \text{mass of } Fe_3O_4/\text{total liposomes} \times 100\%.$$

Gel retardation assay

Agarose gel electrophoresis was used to test the SIRPα siRNA-carrying capacity of FA-PFNB nanoparticles [33]. First, SIRPα siRNA was incubated with FA-PFNB at mass ratios of 1:0, 1:1, 1:2, 1:4, 1:8, 1:16, 1:20, and 1:25 for 10 min at 25°C temperature. After that, add 6×loading buffer to the incubated mixture. Using 3% agarose gel at a voltage of 100 V, the sample was subjected to electrophoresis for 30 min. After electrophoresis, the gel was placed in the gel imaging system to observe the band changes of SIRPα siRNA.

In vitro CEUS imaging

To explore the phase transition dynamics of PNB-SIRPα siRNA and the function of PFP within this process, PNB-SIRPα siRNA nano/microbubbles and nano/microparticles loaded with SIRPα siRNA underwent LIFU exposure at varied acoustic intensities (ranging from 0 to 1.5 W/cm^2, 50% duty cycle). The irradiation lasted different durations from 1 to 4 min. B-mode and contrast-enhanced ultrasound (CEUS) modes were utilized for

Li *et al. Journal of Nanobiotechnology*   (2024) 22:605

Page 5 of 26

image capture, and pre-irradiation images were compared with them as controls. Image analysis and evaluation were conducted using ultrasound imaging software (FDY-II; Institute of Ultrasound Imaging, Chongqing, China). Optical microscopy (DMIL LED Fluo, Leica, Germany) under the optimal ultrasound parameters allowed for the visualization and detection of the phase transition of PNB-SIRPα siRNA.

Cells and animals

The RAW264.7 cell line (representing M0-like macrophages) and Lewis's lung cancer (LLC) cell line used in this study were obtained from Procell Life Science & Technology Co., Ltd. (Wuhan, China). LLC cells were cultured in DMEM supplemented with 10% FBS and 1% penicillin–streptomycin. The cells were incubated in a humidified atmosphere at 37 °C with 5% CO_2. C57BL/6 female mice aged 5–6 weeks were procured from Lanzhou Veterinary Research Institute, Chinese Academy of Agricultural Sciences Co. Ltd. (Lanzhou, China). All mouse experiments were conducted per the approved guidelines by the Ethics Committee of Lanzhou University Second Hospital.

Cell viability assays

The Cell Counting Kit-8 (CCK-8) assay was used to evaluate different concentrations and groups of NBs biocompatibility with RAW264.7 cells and assess the cytotoxicity of different ultrasound parameters on RAW264.7 and LLC cells [34]. Varying concentrations (25–400 μg/mL) and other groups of NBs were introduced into the culture medium of RAW264.7 cells, and the cells were further incubated for an additional 24 h. RAW264.7 cell viability assays were then performed. RAW264.7 and LLC cells were subjected to a range of ultrasound power (0–1.5 W/cm^2) for 1 to 4 min. Following a 24-h incubation, cell viability was assessed using the CCK-8 kit. Subsequently, the PNB-SIRPα siRNA and FA-PFNB-SIRPα siRNA groups were exposed to varying ultrasound parameters at the specified concentrations, followed by the evaluation of cell viability.

Evaluation of transfection efficiency of NBs loading PNB-SIRPα siRNA

To determine the optimal gene transfection parameters using LIFU, various factors, such as ultrasound intensity and duration of irradiation were investigated. The PNB-SIRPα siRNA was incubated with cells for 10 min in a cell incubator before exposure to LIFU at different ultrasound parameters (0–1.5 W/cm^2, duty cycle of 50%). The duration of ultrasound exposure varied from 1 to 4 min. Before ultrasound treatment, the M2-like macrophages were cultured for an additional 6 h, and then the medium

was replaced before continuing the culture for another 24 h. Transfection efficiency was evaluated in the cells through flow cytometry (CytoFLEX, Beckman Coulter, USA) analysis using Cy5-NC/SIRPα siRNA.

Cellular uptake/transfection

M2-like macrophages (2×10^6 cells/pores) were plated onto confocal dishes and incubated at 37 °C. Various media (PBS, free Cy5-SIRPα siRNA [120 nM], Lipo-Cy5-SIRPα siRNA, PNB-Cy5-SIRPα siRNA, PFNB-Cy5-NC siRNA, FA-PFNB-Cy5-SIRPα siRNA, and FA-PFNB-Cy5-SIRPα siRNA + US [200 μg/mL, Cy5-SIRPα siRNA: 120 nM]) were added to the dishes and cells were cultured for 24 h. The ultrasonic treatment process remained unchanged as described earlier for FA-PFNB-Cy5-SIRPα siRNA + US. Following incubation, cell nuclei were stained with DAPI, and images were captured using a laser confocal scanner [35].

M2-like macrophages (2×10^6 cells/pores) were prepared. Different medium conditions were used (PBS, free Cy5-SIRPα siRNA [120 nM], Lipo-Cy5-SIRPα siRNA [120 nM], PNB -Cy5-SIRPα siRNA, PFNB-Cy5-SIRPα siRNA, FA-PFNB-Cy5-SIRPα siRNA and FA-PFNB-Cy5-SIRPα siRNA + US [200 μg/mL, Cy5-SIRPα siRNA: 120 nM]), the ultrasonic treatment method is the same as above. After 24 h of culture, the cells were examined for nanomaterial uptake by flow cytometry, and the results were analyzed using FlowJo software.

Downregulation of SIRPα gene expression after treatment

M2-like macrophages (2×10^6 cells/well) were plated and cultured overnight. Various media formulations were then added to the cells: PBS, Lipo-SIRPα siRNA, PNB-SIRPα siRNA, FA-PNB-SIRPα siRNA, FA-PFNB-SIRPα siRNA, and FA-PFNB-SIRPα siRNA + US (200 μg/mL, SIRPα siRNA: 120 nM). Lipofectamine RNAiMAX Reagent was used as a positive control for SIRPα siRNA delivery. The ultrasonic treatment procedure remained consistent, as described earlier. After an additional 48-h incubation, a Western blot analysis was conducted to evaluate the levels of SIRPα protein expression.

Evaluation of the repolarization of M2-like macrophages

M2-like macrophages were cultured with varying concentrations of PFNB-NC siRNA for 24 h. Subsequently, the macrophages were washed thrice. The M2-like macrophage samples were immediately collected and stained by fluorescence-labeled antibodies, i.e., PE-CD206 and FITC-CD86. The samples were run on a flow cytometer [36].

M2-like macrophages (2×10^6 cells/pores) were inoculated into 6-well plates and received different treatments (PBS, PNB-SIRPα siRNA, PFNB-SIRPα siRNA, FA-PFNB

Li *et al. Journal of Nanobiotechnology*   (2024) 22:605

Page 6 of 26

-SIRPα siRNA and FA-PFNB-SIRPα siRNA + US, (200 µg/mL, other groups with the equivalent Fe_3O_4 or SIRPα siRNA (120 nM) content) based on the LIFU (1W/cm^2, 2min). After 24 h, the cells were stained with fluorescence-labeled antibodies, i.e., PE-CD206 and FITC-CD86 for fluorescence observation. Similarly, the quantized fluorescence intensity was also detected by flow cytometry.

Macrophage-associated cytokine secretion analysis
M2-like macrophages (2×10^6 cells/well) were treated with different formulations in the culture medium, including PBS, PNB-SIRPα siRNA, PFNB-NC siRNA, PFNB-SIRPα siRNA, FA-PFNB-SIRPα siRNA, and FA-PFNB-SIRPα siRNA + US. They were cultured at 37 °C for 24 h to obtain treated macrophages. RT-PCR analysis was performed to assess Interferon-γ(IFN-γ), tumor necrosis factor-α(TNF-α) and Interleukin-10(IL-10) expression levels [37].

Phagocytosis assay
M2-like macrophages (2×10^6 cells/well) were pre-treated with various substances: PBS, PNB-SIRPα siRNA, PFNB-NC siRNA, PFNB-SIRPα siRNA, FA-PFNB-SIRPα siRNA, and FA-PFNB-SIRPα siRNA + US (200 µg/mL). Additionally, all groups were exposed to equivalent Fe_3O_4 or SIRPα siRNA (120 nM) for 48 h. Subsequently, CFSE-labeled LLC cells (5×10^5) were added to the macrophage-containing plate at a 4:1 cell ratio. Following a 6-h incubation, the macrophages were stained with APC-F4/80, and the ratio of double-positive cells (CFSE/APC) within the total macrophage population (APC) was determined using flow cytometry [38].

Apoptosis assays
M2-like macrophages were treated with a different medium condition for 48 h (PBS, PNB-SIRPα siRNA, PFNB-NC siRNA, PFNB-SIRPα siRNA, FA-PFNB-SIRPα siRNA and FA-PFNB-SIRPα siRNA + US). 5×10^5 LCC cells were suspended in 500 µL of M2 conditioned medium in different conditions without FBS. Cell apoptosis was evaluated using the Annexin V-FITC Apoptosis Detection Kit I [39].

Migration and invasion experiment
Cell Migration and invasion tests were performed using a 24-well Transwell (8 µm aperture) plate precoated with matrix glue [40]. 5×10^5 LLC cells were suspended in M2 conditioned medium (PBS, PNB-SIRPα siRNA, PFNB-NC siRNA, PFNB-SIRPα siRNA, FA-PFNB -SIRPα siRNA and FA-PFNB-SIRPα siRNA + US) with different conditions without FBS and added to the upper chamber, and 600 µL RPMI 1640 containing 20% FBS was added to the lower chamber. After a 24-h culture, the matrix glue and residual cells in the upper chamber were removed using a cotton swab. Matrix glue was used in the upper layer of the invasion assay, and no matrix glue was used for migration experiments. The cells beneath the membrane were fixed with a 4% paraformaldehyde fixative for 30 min, followed by staining with 0.5% crystal violet for 10 min and subsequent washing thrice. Finally, the cells passing through the membrane are observed with an optical microscope, counted, and photographed.

Cell proliferation inhibition experiment
LLC cells were inoculated into 6-well plates at a density of 3×10^3 cells per well and cultured overnight at 37 °C. Different conditions of M2-like macrophages conditioned medium (PBS, PNB-SIRPα siRNA, PFNB-NC siRNA, PFNB-SIRPα siRNA, FA-PFNB -SIRPα siRNA, and FA-PFNB-SIRPα siRNA + US) were used, and the medium was changed every two days. After 7 days of treatment, the cells were fixed with 4% paraformaldehyde and stained with 0.5% crystal violet. The fixed and stained cells were then evaluated and documented using biological microscopy to determine the proliferation status of the different cell groups [41].

In vivo fluorescence imaging
To establish the NSCLC tumor-bearing mouse model, 5×10^7 LLC cells in 200 µL of PBS were injected subcutaneously into the right thigh of female C57BL/6 mice (6–8 weeks old). When the tumor volume of the mice grew to approximately 800 mm^3, they were intravenously administrated with PFNB-Cy5-SIRPα siRNA, FA-PFNB-Cy5-SIRPα siRNA via tail vein (injection dose of NBs: 200 µL, 3 mg/mL). At 1, 2, 4, 8, and 24 h, the fluorescence biodistribution of Cy5 in the tumor was analyzed. In the FA-PFNB-Cy5-SIRPα siRNA group, the highest fluorescence aggregation time was given to the LIFU stimulation (1 W/cm^2, 2 min, 50% duty cycle) to observe the in vivo imaging effect. At the peak of fluorescence intensity, the mice were euthanized, and organs, including the heart, liver, spleen, lung, kidney, and tumors, were harvested. These tissues underwent ex vivo imaging for Cy5 fluorescence using the IVIS Spectrum Imaging System (VISQUE Invivo Smart-LF) [42].

In vitro and in vivo PA imaging
To determine the optimal excitation wavelength, we used FA-PFNB-SIRPα siRNA (200 µg/ml, 10 µL) for continuous photoacoustic imaging (Vevo LAZR Photoacoustic Imaging System) (VisualSonics Inc., Toronto, Canada) of the nanomaterials across the excitation wavelength spectrum of 680–970 nm) [43]. When the tumor volume of the mice grew to approximately 800 mm^3, the model rats were randomly divided into three groups

for PA imaging: PFNB-SIRPα siRNA, FA-PFNB-SIRPα siRNA, and FA-PFNB-SIRPα siRNA + US. The drugs were administered to the groups via tail vein injections (injection dose of NBs: 200 μL, 3 mg/mL). The FA-PFNB-SIRPα siRNA + US group underwent LIFU treatment for 2 min with 1 W/cm^2 in 2 h after administering the drug. PA images were acquired after injection at 1 h, 2 h, 4 h, 8 h and 24 h.

In vivo US imaging

The effect of PFNB-Cy5-SIRPα siRNA, FA-PFNB-Cy5-SIRPα siRNA nanocomplexes on in vivo CEUS imaging was tested using an LLC subcutaneous tumor model. When the tumor volume of mice grew to approximately 800 mm^3, CEUS imaging was performed by intravenous injection of nanocomplex solution [44]. The drug was injected through the tail vein and received different treatments (injection dose of NBs: 200 μL, 3 mg/mL). LIFU stimulation was given 2 h after the tail vein injection, and further contrast-enhanced ultrasound was performed. The B-mode and CEUS images were captured before and after LIFU irradiation, and the intensity of the Region of Interest (ROI) was subsequently compared.

In vivo combination cancer therapy

The NSCLC tumor-bearing C57BL/6 mice model (approximately 200 mm^3) was randomly divided into seven groups and treated with various interventions (injection volume: 200 μL, PBS: 10 mM; PNB -SIRPα siRNA, PFNB–NC siRNA, PFNB -SIRPα siRNA, FA-PFNB-SIRPα siRNA, FA-PFNB-SIRPα siRNA + US, and (PNB-SIRPα siRNA + PFNB-NC siRNA) (injection dose of NBs: 200 μL, 3 mg/mL). Tumor volume was monitored using a vernier caliper. Survival analysis was performed on the mice, and continuous observation was performed until the 35th day. In addition to the spontaneous death of the mice, when the tumor volume reached 2000 mm^3, or the length of the tumor was > 20 mm, it could also be considered the death endpoint.

Intertumoral lymphocyte analysis

On the 14th day after the treatment, the mice in each group were euthanized, and tumor tissues and draining lymph nodes were extracted to prepare a single-cell suspension for analyzing the tumor immune microenvironment [45]. To assess SIRPα expression on the macrophage surface, macrophages were labeled with anti-F4/80-APC and anti-SIRPα-FITC antibodies for flow cytometric analysis. To analyze cytotoxic T lymphocytes (CTLs, CD3CD4, CD3CD8), T lymphocytes were stained with anti-CD3-PE, anti-CD4-FITC, and anti-CD8-FITC antibodies. For assessing T cell activation and proliferation frequency, lymphocytes were stained

with anti-CD4-FITC, anti-CD8-FITC, anti-CD69-PE, anti-IFN-γ-PE, and anti-ki67-PE antibodies. The frequency of regulatory T cells (Tregs) (CD4 Foxp3) was analyzed by staining lymphocytes with anti-CD4-FITC and anti-Foxp3-PE antibodies. M2-like macrophages (F4/80CD206) and M1 macrophages (F4/80CD86) in tumor tissue cell suspensions were identified using anti-F4/80-APC, anti-CD86-FITC, and anti-CD206-PE antibodies through flow cytometric analysis. TNF-α and IFN-γ levels in tumor tissues were determined using enzyme-linked immunosorbent assay (ELISA). Subsequently, the frequency of M1-like macrophages (F4/80CD86), CTLs (CD3CD4, CD3CD8), and T cell activation and proliferation (CD4 IFN-γ, CD8 IFN-γ, CD8Ki67) in the tumor-draining lymph nodes (TDLNs) was examined using flow cytometric analysis [36, 46].

Detection of apoptosis in tumor tissues

TUNEL staining was performed to detect post-treatment apoptosis in tumor tissue. The stained sections were examined under a fluorescence microscope (Olympus, Japan) to identify apoptosis. The apoptotic index was determined and analyzed in five randomly selected samples. Additionally, tumor tissues were stained with hematoxylin and eosin (H&E) to assess the pathological alterations [47].

Transcriptomic analysis

The NSCLC tumor-bearing mice were divided into PBS and FA-PFNB-SIRPα siRNA + US groups. After treatment completion, tumor tissues were collected for transcriptome sequencing analysis [48].

In vitro assays for immune cell stimulation

Primary murine spleen-derived lymphocytes (PBMC) were isolated according to previously described protocols [49]. The collected primary lymphocytes were added to the three groups with different treatments: PBMC + LLC + M0 group, PBMC + LLC + M2(PBS) group, PBMC + LLC + M2(FA-PFNB-SIRPα siRNA + US). The cells were co-cultured for 24 h, and lymphocytes were stained with anti-CD8-FITC, anti-CD69-PE, anti-CD4-FITC, and anti-CD69-PE, as well as anti-CD8-FITC and anti-Ki67-PE to assess lymphocyte activation and proliferation via flow cytometry. Additionally, supernatants from stimulated lymphocytes were collected and used to culture LLC cells for 24 h. Following incubation, LLC cell viability and apoptotic rate were assessed using the CCK-8 assay and an apoptosis kit.

Toxicity assessment

A histopathological evaluation of vital organs was conducted to assess potential toxicity from various

Li *et al. Journal of Nanobiotechnology*   (2024) 22:605

Page 8 of 26

treatments. Heart, liver, spleen, lung, and kidney specimens were harvested from each group of mice, fixed in paraffin, and sectioned for hematoxylin and eosin (H&E) staining. Observations and evaluations of the stained sections were carried out using a light microscope. Blood samples were collected from the mice for routine tests. Following overnight refrigeration at 4 °C, serum samples were obtained by centrifugation and analyzed for key serological biochemical indicators using an automated analyzer (Hitachi High-Technologies Corp., Japan).

Statistical analysis

Statistical analysis was conducted using GraphPad Prism 7 (GraphPad, San Diego, USA). Student's t-test and one-way analysis of variance (ANOVA) were employed for data analysis. Survival analyses were performed using the Kaplan–Meier method with a log-rank test. All statistical results are presented as mean ± standard error of measurement. Statistical significance was defined as a P-value < 0.05 (*P < 0.05; **P < 0.01; ***P < 0.001; ****P < 0.0001).

Results

Preparation and characteristics of FA-PFNB-SIRPα siRNA

Treatment of RAW264.7 cells with IL-4 led to a notable increase in CD206 expression from 27.00 ± 1.375% to 96.03 ± 1.519%, indicating successful polarization of M0 (RAW264.7) cells into M2-like macrophages (Figure S1). As shown in Figures S2 and S3, we successfully selected siRNA (SIRPα-3) as the best choice for silencing the SIRPα gene. In Fig. 1A, the solution color shifted from milky white to brown upon adding OA-Fe$_3$O$_4$, confirming the successful incorporation of iron. TEM analysis revealed distinct structural variances between FA-PFNB-SIRPα siRNA and FA-PNB-SIRPα siRNA NBs, with iron oxide particles prominently present in the former NBs while absent in the latter group (Figs. 1D, E). The mean diameter of FA-PFNB-SIRPα siRNA was 211.3 ± 1.1 nm (Fig. 1B). Furthermore, the polydispersity index (PDI) of FA-PFNB-SIRPα siRNA was 0.218 ± 0.001, affirming the uniform dispersion and homogeneity of these nanobubbles. The zeta potential of FA-PFNB-SIRPα siRNA was—12.13 mV (Fig. 1C). No significant size changes were observed during the 10-day observation period, indicating the stability of the NBs (Figure S4). The Fe content was determined by atomic absorption spectroscopy (R2 = 0.9981), and the Fe3O4 encapsulation efficiency and loading capacity were calculated to be 73.33 ± 1.03% and 15.49 ± 0.18%, respectively (Figure S5). The positive charge on the DOTAP hydrophilic head of FA-PFNB-SIRPα siRNA facilitates the electrostatic interaction with the siRNA, enabling effective attraction to the nanobubble surface. Additionally, FA-PFNB was detected for gene-carrying capacity through agarose gel electrophoresis (Fig. 1F). During agarose gel electrophoresis, free siRNA in lane 1 exhibited a reduction in brightness when the mass ratio of siRNA to FA-PFNB was 1:20. Remarkably, at a ratio of 1:25, the siRNA bands vanished. To
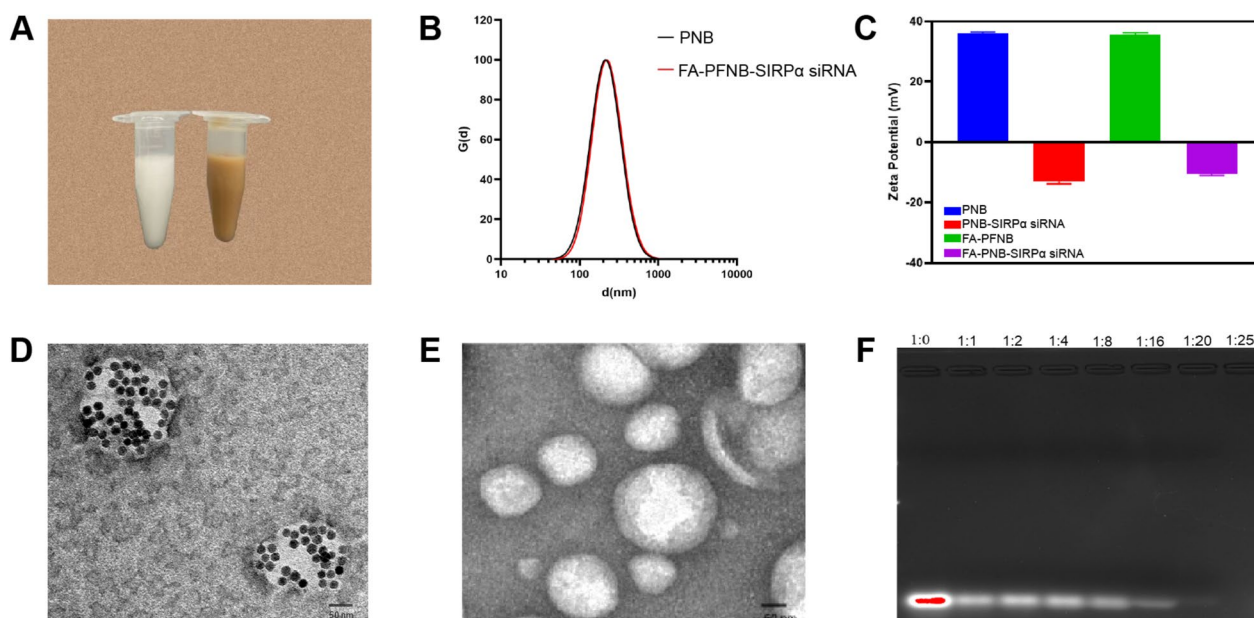

Fig. 1 Characteristics of the FA-PFNB-SIRPα siRNA. **A** Appearance diagram of PNB- SIRP α siRNA versus FA-PFNB-SIRPα siRNA. **B** Size and zeta potential (**C**) of FA-PFNB-SIRPα siRNA. **D**, **E** The Transition electron microscope image of FA-PFNB-SIRPα siRNA and PNB-SIRPα siRNA. **F** Agarose gel electrophoresis assay of the FA-PFNB loaded SIRPα siRNA. SIRP α, signal regulatory protein α; FA, folic acid

Li *et al. Journal of Nanobiotechnology*   (2024) 22:605

Page 9 of 26

ensure the safety of nanomaterials, the optimal mass ratio of 1:20 was used in this experiment.

In vitro biosafety assay

The toxicity of varying concentrations of different groups of RAW264.7 cells was determined using the CCK-8 method. Additionally, the effects of different ultrasound parameters on LLC and RAW264.7 cells were investigated. Divided into PNB-SIRPα siRNA, PFNB-NC siRNA, PFNB-SIRPα siRNA, and FA-PFNB-SIRPα siRNA groups, RAW264.7 cells were incubated with different concentrations (25–400 μg/mL). When the concentration of PFNB-NC siRNA, PFNB-SIRPα siRNA group was 400 μg/mL, the cell viability was < 80%. However, 200 μg/mL NBs of all groups had good cell compatibility, and the cell viability was > 85% (Figure S6). Therefore, 200 μg/mL NBs could be used as a reference concentration for cell experiments. Simultaneously, we further found that different ultrasound parameters had no significant effect on the cell viability of LLC and RAW264.7 cells (Figure S7). Subsequently, the cell viability of RAW264.7 cells was tested at 200 μg/mL concentrations of PNB-NC siRNA or FA-PFNB-SIRRP-α siRNA under different ultrasound parameters. The results showed that 200 μg/mL PNB-NC siRNA or FA-PFNB-SIRRP-α siRNA had good biocompatibility under different ultrasonic parameters, and the cell viability was > 80% (Figures S8, S9).

In vitro ADV and US imaging and transfection efficiency assay in M2

CEUS plays a crucial role in the differential diagnosis of tumors [50]. In PNB-SIRPα siRNA, PFP acts due to LIFU-triggered ADV, thus allowing PFP-coated NBs to enhance US imaging. Firstly, Before LIFU irradiation, there were no echoes or very low echo intensities in both B-mode and CEUS modes. However, as the LIFU intensity increased, reaching 1 W/cm^2 with a duration of 1 min, contrast-enhanced ultrasound images began to appear. When the LIFU parameters were 1 W/cm^2 and 2 min, the intensity of the NBs peaked for CEUS (Figs. 2A, C, D). Furthermore, the formation of bubbles in the micrometer scale was observed under the microscope (Fig. 2E), which proved that PFP was successfully coated in the nanoparticles and the phase transition of nanoparticles could be triggered by LIFU (1 W/cm^2, 2 min). In contrast, the echo intensity of NPs-SIRPα siRNA without PFP remained constant irrespective of the LIFU intensity or stimulation time in the B and CEUS modes (Figure S10). All the above results confirmed that PNB -SIRPα siRNA encapsulated PFP can respond well to ADV and thus enhance US imaging performance. Moreover, from an imaging perspective, the optimal LIFU excitation intensity for NBs is 1 W/cm^2 for 2 min.

Compared with other nanoparticles, NBs possess a unique characteristic called "ultrasonic cavitation" induced by ultrasonic irradiation [51]. This phenomenon creates approximately a 300 nm gap in the cell membrane, enhancing cell permeability [52]. In this study, we detected the transfection efficiency of M2-like macrophages with different LIFU intensities and at other times; among them, siRNA was labeled using the red probe Cy5. The LIFU treatment (1 W/m^2, 2 min, and duty cycle of 50%) exhibited the highest transfection efficiency at 75.82 ± 0.64%, compared to the control group at 49.83 ± 0.78% (Fig. 2B, F). Thus, the optimal parameters for achieving the highest transfection efficiency were an ultrasound intensity of 1 W/m^2 and an irradiation time of 2 min.

The transfection efficiency of US combined with FA-PFNB-SIRPα siRNA on M2-like TAM was further verified. It was found that almost all of the cells in the US combined with the FA-PFNB-Cy5-SIRPα siRNA group had red fluorescence signals (Fig. 2G). However, it was difficult for free Cy5-siRNA to enter the cells (Figure S11). Flow cytometry was used to further evaluate the transfection efficiency of M2-like macrophages. In the US combined with the FA-PFNB-Cy5-SIRPα siRNA group, the cell uptake rate was > 95%, consistent with the confocal image results (Fig. 2H and I). FRβ expression was also detected in M0 and M2 mouse umbilical vein endothelial cells (MUVEC). Flow cytometry results confirmed that M2-like macrophages exhibited a higher mean fluorescence intensity than M0 and MUVEC cells (Figure S12). This outcome can be ascribed to the presence of FA on the surface of FA-PFNB-SIRPα siRNA, facilitating the uptake of nanomaterials by M2-like macrophages through specific binding to the overexpressed FRβ. Furthermore, the cavitation effect of ultrasound augmented the uptake of nanobubbles by macrophages.

Delivery of Fe_3O_4 and SIRP α siRNA in FA-PFNB regulated the polarization of macrophages

Despite the tumor diversity, M2-like macrophages expressing CD206 share common features linked to angiogenesis and the inhibition of anti-tumor immune responses. These characteristics bolster the advancement and metastasis of various cancer types [53]. In this study, we incubated M2-like macrophages with PFNB-NC siRNA at different concentrations and found that the expression of M1-like macrophage marker CD86 was gradually increased, and CD206 was progressively decreased with increasing concentrations (The active ingredient was nano-Fe_3O_4; hence PNB-NC siRNA did not significantly impact on M2-like macrophages (Figures S13, S14). However, when the concentration was 200 μg/mL and 300 μg/mL, there was no significant

1:PBS   **2:Lipo-Cy5-SIRPα siRNA**   **3:PNB-Cy5-SIRPα siRNA**
4:PFNB-Cy5-NC siRNA   **5:FA-PFNB-Cy5-SIRPα siRNA**   **6:FA-PFNB-Cy5-SIRPα siRNA+US**

Fig. 2 In vitro ultrasound imaging and transfection efficiency of different conditions. **A** Ultrasound imaging (left: B-Mode, right: contrast-enhanced ultrasound) of PNB-SIRPα siRNA. **B**, **F** Transfection efficiency for different ultrasound parameters. **C**, **D** Quantitative analysis of PNB-SIRPα siRNA echo intensity following LIFU irradiation at various intensities and durations in B-mode (**C**) and CEUS mode (**D**). **E** Phase change microscopy image of PNB-SIRPα siRNA (scale bar = 10 μm). **G** Laser confocal microscope images of the M2-like macrophage uptake of different nanocarriers (scale bar = 100 μm). **H**, **I** The transfection efficiency of different nanocarriers by flow cytometry. Data was presented by the mean ± SD (n = 3) per group. *$P < 0.05$; **$P < 0.01$; ***$P < 0.001$; ****$P < 0.0001$

difference in the expression levels of CD86 and CD206, respectively (Figures S15, S16). This indicates that Fe_3O_4 has a limited ability to re-educate M2, and it needs to

be used together with other therapies. Subsequently, we observed a significant upregulation of IRF5 expression in M2-like macrophages following the addition of

Li *et al. Journal of Nanobiotechnology*   (2024) 22:605

Page 11 of 26

PFNB-NC siRNA compared to M2-like macrophages alone and M2+PNB-NC siRNA (Figure S18). Therefore, remodeling M2-like macrophages by Fe_3O_4 may be related to the activation of the IRF5 pathway. However, SIRPα gene knockdown did not affect IRF5 in M2-like macrophages, indicating no crosstalk between SIRPα-mediated pathways and IRF5 (Figure S17). Furthermore, the efficiency of different groups in silencing SIRPα of M2-like macrophages was assessed using Western blotting assays. Fig. 3A and B demonstrate a substantial decrease in SIRPα expression in M2-like macrophages following treatment with both FA-PFNB-SIRPα siRNA+US and Lipo-SIRPα siRNA. The FA-PFNB-SIRPα siRNA+US group showed the most significant reduction in expression, which decreased by > 80% compared with the control group. There was no significant difference between FA-PNB-SIRPα siRNA (no Fe_3O_4) and FA-PFNB-SIRPα siRNA (including Fe_3O_4), indicating that Fe_3O_4 did not affect the expression of SIRPα. We also found that all treatment groups significantly reshaped M2-like macrophages into M1, while the FA-PFNB-SIRPα siRNA+US group had the highest proportion of M1-like macrophages and the lowest proportion of M2 (Fig. 3C–F). Moreover, the highest expression levels of inflammatory cytokines IFN-γ and TNF-α in macrophages were FA-PFNB-SIRP α siRNA+US group, and the lowest expression levels of the immunosuppression-related IL-10 were also FA-PFNB-SIRPα siRNA+US group (Fig. 3H–J). Among them, Fe_3O_4 promotion of the polarization of macrophages may be by upregulating IRF5, while SIRPα knockout promotes the M1-like polarization of macrophages, which may be related to the reduction of SHP-1/p38MAPK/STAT3 [54].

Delivery of Fe_3O_4 and SIRPα siRNA in FA-PFNB regulates the phagocytic efficiency of macrophage
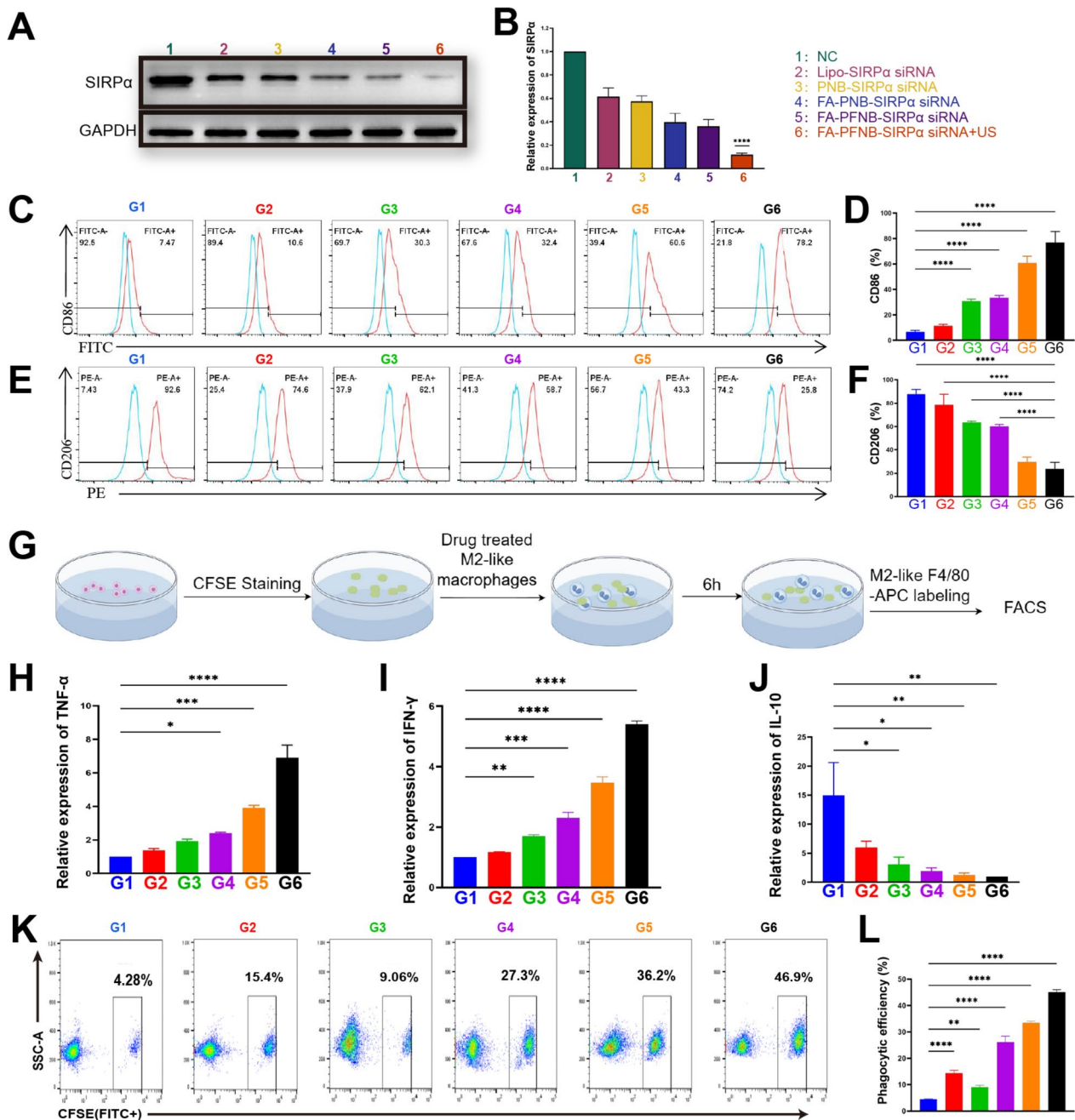
To investigate whether US combined with FA-PFNB-SIRP α siRNA could enhance the phagocytic efficiency of M2-like macrophages for tumor cells, M2-like macrophages were pretreated with different groups for 48 h and then co-cultured with CFSE-labeled LLC cells for 6 h. Next, macrophages were stained with APC-labeled F4/80 antibody, and cellular phagocytosis was measured by flow cytometry (Fig. 3G). The phagocytosis ratio of M2 macrophages treated with PNB-SIRPα siRNA (14.37±1.04%) was higher than that of PBS-treated group (4.43±0.20%) (Fig. 3K-L), which may be attributed to the inhibition of CD47/SIRPα interactions by the linked SIRPα siRNA on the liposome. M1-like macrophages generally show improved phagocytosis of tumor cells compared to M2. An enhanced proportion of phagocytosis was also observed in M2-like macrophages treated with PFNB-NC siRNA (9.00±0.78%), consistent with previous studies [15, 51]. Under the dual effect of Fe_3O_4 and SIRPα siRNA, for PFNB-SIRPα siRNA (26.17±2.21%), the proportion of phagocytosis induced by Fe_3O_4 and SIRPα siRNA was higher than that of PNB-SIRPα siRNA and PFNB-NC siRNA group. Notably, the phagocytosis of LLC by macrophages in the FA-PFNB-SIRPα siRNA group (33.4±0.66%) showed a significant increase compared to the PFNB-SIRPα siRNA group. However, the FA-PFNB -SIRPα siRNA+US group showed the highest proportion of phagocytosis (45.07±0.95%), which may be related to the cavitation and sonoporation effects of ultrasound to promote the uptake of targeted nanobubbles.

TAMs treated with FA-PFNB-SIRPα siRNA combined with US effectively inhibit NSCLC migration, invasion and proliferation and promote NSCLC apoptosis

Disrupting the M2-induced polarization of TAMs can impede tumor invasion and metastasis [55, 56]. We employed a transwell assay for validation to investigate the impact of FA-PFNB-SIRPα siRNA+US treatment on inhibiting the invasion and metastasis of LLC cells in vitro. After 48 h of treating M2-like TAMs in various groups, we collected and applied the conditioned medium to LLC cells. The FA-PFNB-SIRPα siRNA+US group exhibited reduced cell migration and invasion abilities compared to the control and other groups. At the 24-h mark, the transwell migration assays revealed a significant decrease in cell migrations of the FA-PFNB-SIRPα siRNA+US group compared to others ($P < 0.01$), with only one-fifth of the migrated cells observed in the control group (Fig. 4A, B). Similarly, the transwell invasion assay demonstrated that after 24 h, only a small number of cells from the FA-PFNB-SIRPα siRNA+US group traversed the chamber, whereas the control group had nearly 6.9 times more cells passing through (Fig. 4C, D). Therefore, combining US and FA-PFNB-SIRPα siRNA can effectively inhibit NSCLC invasion and metastasis, potentially by altering the polarization of M2-like TAMs.

In line with the transwell assay findings, flow cytometry results (Fig. 4E, F) demonstrated a notable rise in the apoptosis of LLC tumor cells when exposed to the conditioned medium of M2-like TAMs treated with US in conjunction with FA-PFNB-SIRPα siRNA, as opposed to the PBS group. Approximately 39.37±1.62% and 46±1.41% of the cells in the FA-PFNB-SIRPα siRNA and FA-PFNB-SIRPα siRNA+US (the highest apoptotic rate) groups, respectively, went into apoptosis. This effect may arise from the ability of US, in conjunction with FA-PFNB-SIRPα siRNA, to enhance the uptake of nanocomposites by macrophages. This, in turn, increases intracellular levels of Fe_3O_4 and SIRPα siRNA, facilitating the repolarization of M2-like TAMs to an M1 phenotype.

Fig. 3 In vitro gene silencing of macrophages and polarization and phagocytosis efficiency assays. **A**, **B** Western blotting (**A**) and (**B**) relative quantitative analyses of SIRP α Protein expression in different groups of M2-like macrophages. **C**–**F** M1-like marker (i.e., CD 86) and M2-like macrophage marker (i.e., CD206) expression of different groups by flow cytometry. **G** Schematic showing the procedures. **H-J** IFN-γ, TNF-α, and IL-10 mRNA expression by quantitative RT-PCR. **K**, **L** Flow cytometric analysis of the phagocytosis of LLC cells in different groups of macrophages. Data are presented as mean ± SD (n = 3) per group. *$P < 0.05$; **$P < 0.01$; ***$P < 0.001$; ****$P < 0.0001$

To further test the long-term efficacy of US combined with targeted nanocomposite therapy, we performed colony-forming assays in which conditioned medium was obtained from M2-like macrophages treated with various treatments, followed by LLC cells pretreated and cultured for an additional 7 days. The cell colony formation was notably decreased in the FA-PFNB-SIRPα siRNA and PFNB-SIRPα siRNA groups
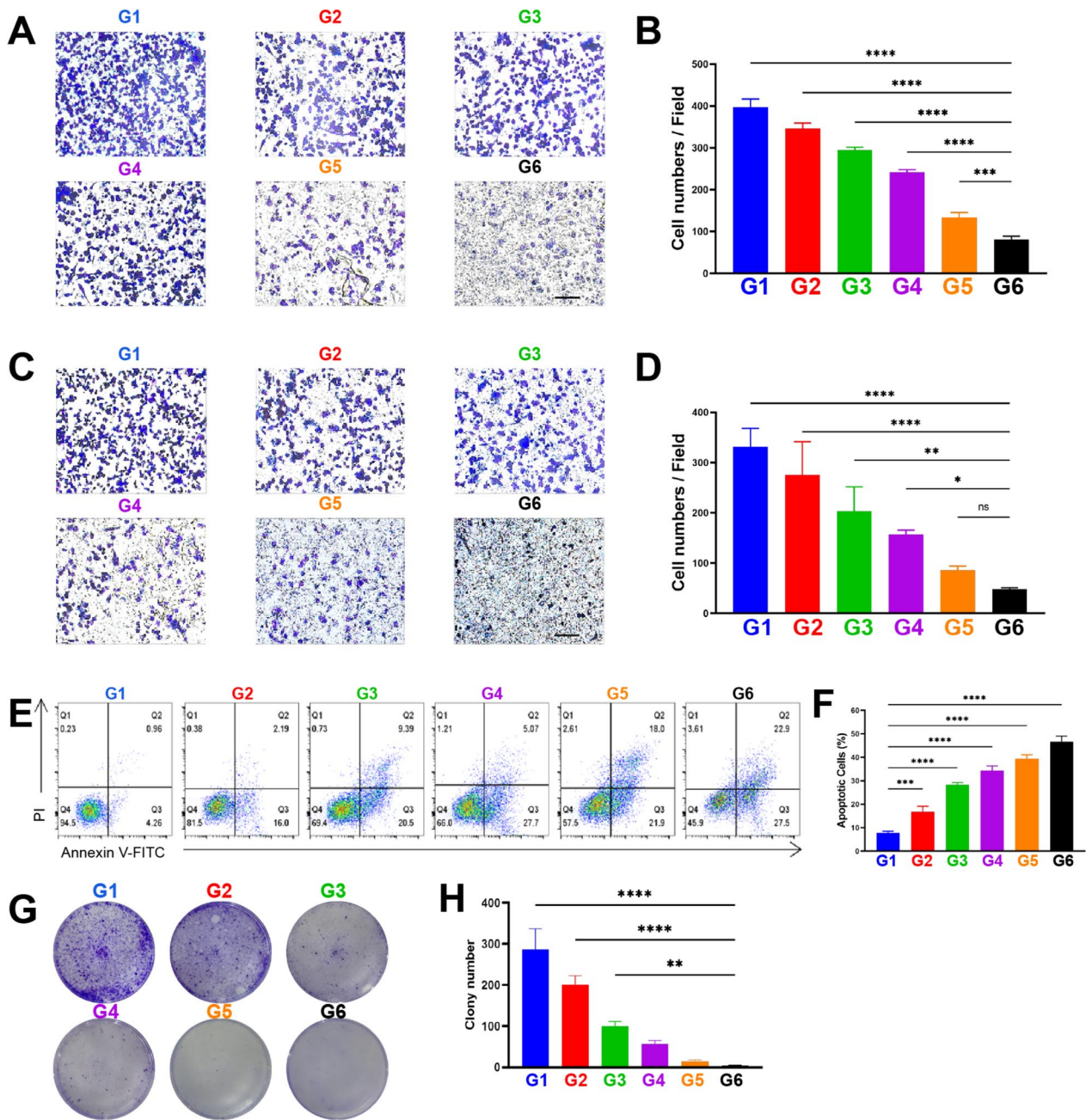
G1:PBS   G2:PNB-SIRPα siRNA   G3:PFNB-NC siRNA   G4:PFNB-SIRPα siRNA   G5:FA-PFNB-SIRPα siRNA   G6:FA-PFNB-SIRPα siRNA+US

Fig. 4 Invasive metastasis assay of non-small cell lung cancer cells (LLC) under different conditioned media. **A**, **B** The migration ability of LLC cells under different M2-like macrophages conditioned media was detected by transwell migration assays (scale bar = 100 μm). **C**, **D** Cell invasion ability of LLC cells under different M2-like macrophage-conditioned media was detected by transwell invasion assays (scale bar = 100 μm). **E**, **F** Apoptosis assay of LLC cells under different M2-like macrophage conditioned media. **G**, **H** Colony-forming assays of LLC cells under different M2-like macrophage-conditioned media. Data was presented by the mean ± SD (n = 3) per group. *$P < 0.05$; **$P < 0.01$; ***$P < 0.001$; ****$P < 0.0001$

compared to the Control group, as well as the PFNB-NC siRNA and PNB-SIRPα siRNA groups (Fig. 4G, H). However, the number of cell colonies irradiated with FA-PFNB-SIRPα siRNA combined with US was further reduced. The reduction in the colony formation efficiency of LLC cells was most pronounced when ultrasound was combined with FA-PFNB-SIRPα siRNA, decreasing to < 10%.

Li *et al. Journal of Nanobiotechnology*   (2024) 22:605

Page 14 of 26

FA-PFNB-SIRPα siRNA + US promotes the enrichment of nanobubbles in tumor tissues and has a good therapeutic effect

We conducted a detailed exploration of the NSCLC tumor-bearing mouse model distribution of folate-targeted and ultrasound-targeted NBs. Fluorescence intensity at the tumor site reached a maximum at 2 h after injection at PFNB-Cy5-SIRPα siRNA or FA-PFNB-Cy5-SIRPα siRNA group. However, the fluorescence signal was significantly stronger in the FA-PFNB-Cy5-SIRPα siRNA group than in the PFNB-Cy5-SIRPαsiRNA group at all time points (Fig. 5A, B). At 2 h post-injection, major organs and tumor tissues were isolated and imaged. FA-PFNB-Cy5-SIRPα siRNA-treated mice showed stronger Cy5 fluorescence in tumor tissues, indicating a more efficient tumor aggregation of FA-targeted nanoparticles (Fig. 5C, D). After 2 h of FA-PFNB Cy5-SIRPα siRNA injection, the mouse tumor was subjected to LIFU (1 W/cm^2, 2 min). The tumor site showed a stronger fluorescence value than the FA-PFNB-Cy5-SIRPα siRNA group, and reached the peak at 4 h. Simultaneously, following 4 h of ex vivo organ imaging, the fluorescence intensity at the tumor tissues was notably higher than the peak of FA-PFNB-Cy5-SIRPα siRNA group.

Photoacoustic (PA) imaging harnesses optical resolution, offering wide-ranging possibilities for preclinical and clinical settings, and Fe$_3$O$_4$ has applications in PA imaging. In our experiment, FA-PFNB-SIRPα siRNA was scanned across the spectrum from 680 to 950 nm to identify the peak absorbance. The peak detected at 690 nm, consistent with previous findings [56], was selected for subsequent PA imaging (Figure S19). PA imaging was performed on NSCLC tumor-bearing mice in vivo after the intravenous injection of FA-PFNB-SIRPα siRNA or PFNB-SIRPα siRNA, and PA values were quantified. Both had noticeable PA signals at the tumor site, suggesting that the NBs effectively accumulate in the tumor tissue; however, the FA-PFNB-SIRPα siRNA was significantly higher. Moreover, LIFU administered at 2 h post-intravenous injection notably amplified the PA signal at the tumor site in mice (Fig. 5E, F). This suggests that LIFU effectively enhanced the accumulation of Fe$_3$O$_4$ in the deep-seated tumor tissue, aligning with the in vivo animal imaging findings.

Referring to the biodistribution of NBs in vivo as described previously, the time point of 2 h NBs after injection was selected for observation, and no obvious CEUS was observed in either the FA-PFNB-SIRPα siRNA or PFNB-SIRPα siRNA groups (Fig. 5G). However, after LIFU irradiated (1 W/cm^2, 2 min), the FA-PFNB-SIRPα siRNA group showed a hyperintense signal in the lesion site under CEUS mode, which was significantly higher than that in the PFNB-SIRPα siRNA group. The results

are consistent with previous studies and in vivo imaging, indicating that NBs cannot initiate ADV without LIFU stimulation. Similarly, the retention of NBs in the tumor region is reduced if no FA is targeted.

In vivo evaluation of anti-tumor performance

Building on our promising in vitro and in vivo findings, we assessed the therapeutic effectiveness of FA-PFNB-SIRPα siRNA in C57BL/6 mice bearing LLC tumors. The mice were randomly divided into seven groups: PBS, PNB-SIRPα siRNA, PFNB-NC siRNA, PFNB-SIRPα siRNA, FA-PFNB-SIRPα siRNA, FA-PFNB-SIRPα siRNA + US, and PNB-SIRPα siRNA + PFNB-NC siRNA. Treatment was given every 2 days (Fig. 6A). While each treatment group exhibited tumor inhibition capabilities, the FA-PFNB-SIRPα siRNA + US group demonstrated the most potent anti-tumor efficacy (Fig. 6B, C and E). We photographed the tumor tissue to visually verify the superior anticancer activity of the FA-PFNB-SIRPαRNA + US group (Fig. 6F). In addition, we confirmed that the SIRPα gene was silenced after treatment in the FA-PFNB-SIRPα siRNA + US group (Figure S20). Apoptosis was also clearly observed in the FA-PFNB-SIRPα siRNA + US by TUNEL staining (Fig. 6H, I). Moreover, the results of tumor HE staining (Fig. 6J) showed that the necrotic area of tumor cells in each group was significantly higher than that in the PBS group, and the effect of FA-PFNB-SIRPα siRNA + US was relatively stronger. Furthermore, based on the survival rates observed in various treatment groups, it was noted that all mice in the PBS group died after 16 days, whereas the group treated with ultrasound in combination with FA-PFNB-SIRPα siRNA exhibited a 60% survival rate at day 35, demonstrating its superior anti-tumor efficacy (Fig. 6G).

Administration of US combined with FA-PFNB-SIRPα siRNA significantly modified the immunosuppressive TME

To verify the role of TAM polarization in tumors after different treatments, immune-cell populations in the tumor tissue were analyzed, and M1 and M2 macrophages were stained with F4/80、CD86, and CD206 antibodies, respectively (Fig. 7A, B and Figure S21). Compared with the PBS group, the percentage of CD86 positive macrophages (F4/80$^+$CD86$^+$ lymphocytes) was significantly increased, while the percentage of CD206 positive macrophages (F4/80$^+$CD206$^+$ lymphocytes) was significantly decreased in all treatment groups. These results indicate that Fe$_3$O$_4$ NPs and SIRPα knockout can effectively transform TAMs from M2 to M1-type, consistent with the in vitro results. Notably, CD86 expression was highest, and CD206 expression was lowest in the FA-PFNB-SIRPα siRNA + US group. This indicates that FA-PFNB-SIRPα
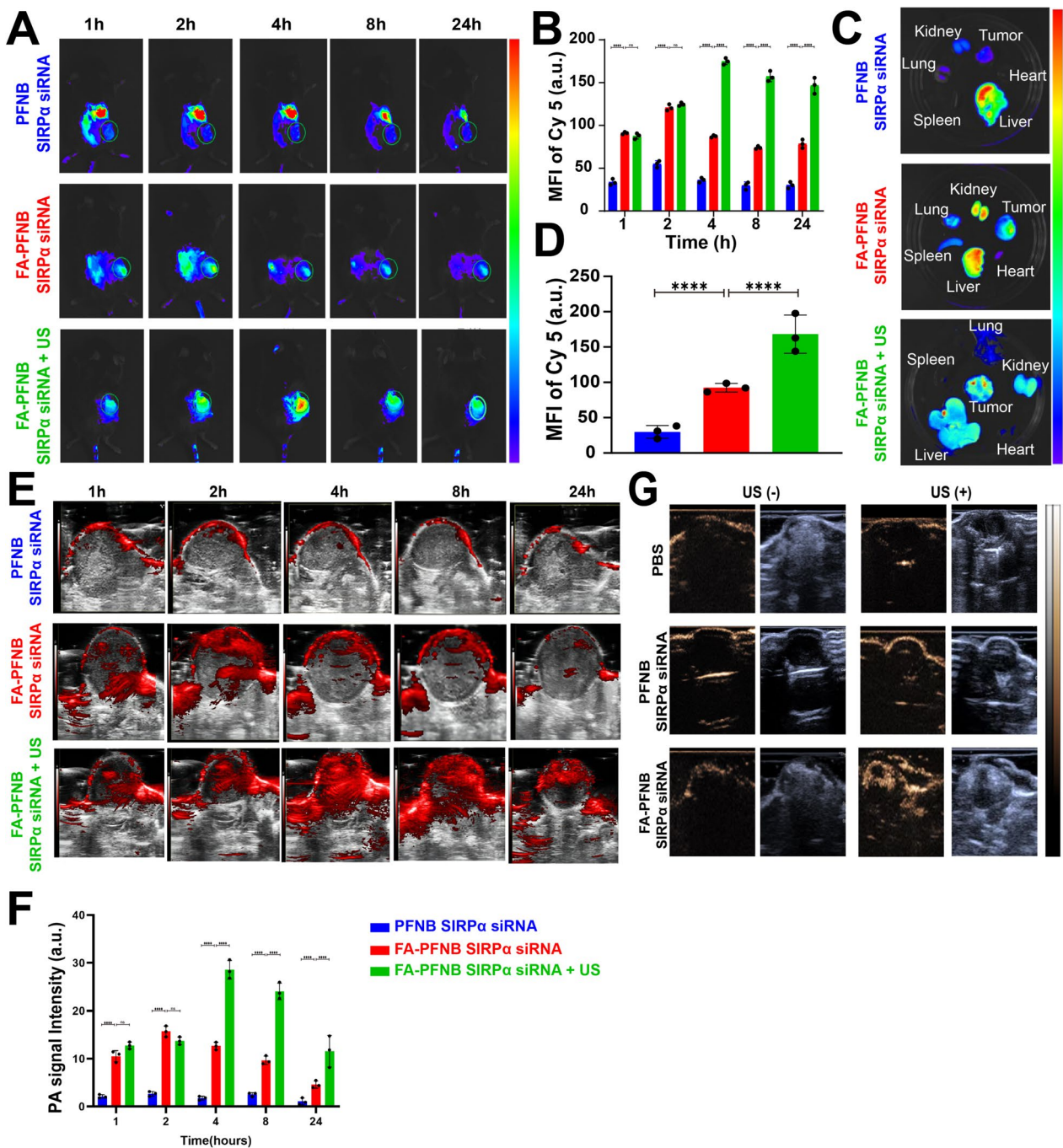
Fig. 5 In vivo multimodal imaging images. **A**, **B** Biodistribution of FA-PFNB-Cy5-SIRPα siRNA in LLC tumor-bearing C57BL/6 mice (Number of replicates, n = 3). **C**, **D** The organs and tumor tissues were imaged at the peak of fluorescence value in vivo (Number of replicates, n = 3). **E**, **F** PA images of the tumors in model rats of PFNB-SIRPα siRNA or FA-PFNB-SIRPα siRNA and FA-PFNB-SIRPα siRNA + US groups (Number of replicates, n = 3). **G** Ultrasound imaging of mice bearing non-small cell lung cancer tumors with different treatment groups in B-mode and CEUS mode before and after Low-intensity focused ultrasound (Number of replicates, n = 3). Data was presented by the mean ± SD (n = 3) per group. *$P < 0.05$; **$P < 0.01$; ***$P < 0.001$; ****$P < 0.0001$. PA, photoacoustic imaging; MFI, mean fluorescence intensity; LIFU, low-intensity focused ultrasound; SIRPα, signal regulatory protein α

siRNA + US can enhance the polarization of M1-like macrophages while suppressing M2-like macrophages within the TME in NSCLC.

In the following step, we examined the abundance of M1-like macrophages and the proliferation and activation of T cells in the TDLN. The level of F4/80$^+$CD86$^+$ in the TDLN of the FA-PFNB-SIRPα siRNA + US group was notably higher than that in other treatment groups (Fig. 7C and S22). IFN-γ or CD69 is mainly secreted by activated CD4 or CD8 T lymphocytes [57].in addition, the expression of Ki67 was a cell-associated protein closely related to effector T cell proliferation and growth [58] Moreover, the levels of CD3$^+$CD4$^+$, CD3$^+$CD8$^+$, CD4$^+$IFNγ$^+$, CD8$^+$IFNγ$^+$, and CD8$^+$ki67$^+$ in the TDLN of the FA-PFNB-SIRPα siRNA + US group were significantly elevated in comparison to the other treatment groups (Fig. 7D–H, S23, 24). These findings suggest that combining US with PFNB-SIRPα siRNA + US demonstrated a superior immunostimulatory effect. Overall, these results indicate that the FA-PFNB-SIRPα siRNA + US treatment led to an increased abundance of M1-like macrophages and enhanced proliferation and activation of T cells in the TDLN. This phenomenon may be attributed to the rise in M1-like macrophages and their enhanced phagocytic activity within the tumor tissues.

Subsequently, tumor-infiltrating CTLs, including CD4$^+$ and CD8$^+$ T cells, were analyzed by flow cytometry to assess the anti-tumor immunity induced by FA-PFNB-SIRPα siRNA + US. The highest CD3$^+$CD4$^+$ and CD3$^+$CD8$^+$ T cell ratios were observed under the combined treatment with FA-PFNB-SIRPα siRNA plus LIFU, which were > 10 times higher than in the PBS group, respectively (Fig. 7I, J, and S25). Significantly elevated levels of CD4$^+$ and CD8$^+$ T lymphocytes were observed in the FA-PFNB-SIRPα siRNA + US group compared to the FA-PFNB-SIRPα siRNA group, potentially due to ultrasound-mediated microbubble destruction (UTMD) enhancing drug delivery for M2-like macrophages. Additionally, it promotes CTL infiltration by modifying M2 and enhancing its phagocytic capacity. All treatment groups activated CD4 and CD8 T cells, while the proportion of IFN-γ$^+$ and CD69 $^+$ in CD4$^+$ T, IFN-γ$^+$ and CD69 $^+$ in CD8$^+$ T cells was the highest in the FA-PFNB-SIRPα siRNA + US group (Figs. 7K–N and S26, S27). The level

of Ki67$^+$ in CD8$^+$ T cells was at its peak after FA-PFNB-SIRPα siRNA + US treatment (Figs. 7O and S28).

Tumor-infiltrating Tregs negatively regulated the response to immunotherapy; hence, reducing the proportion of Tregs in tumors is necessary to ensure the success of immunotherapy. Therefore, we investigated whether FA-PFNB-SIRPα siRNA + US could effectively modify the immunosuppressive TME. As shown in Fig. 7P and Figure S29, the administration of FA-PFNB-SIRPα siRNA to mice with NSCLC significantly inhibited Tregs (Foxp3 T cells gating CD4 T cells) infiltration, which was further reduced in FA-PFNB-SIRPα siRNA + US group. This indicates that immunosuppressive TME was effectively reversed after combined treatment. Furthermore, FA-PFNB-SIRPα siRNA + US treatment resulted in the highest expression levels of anti-tumor related cytokines such as TNF-α and IFN-γ among all groups (Fig. 7Q, R, $P < 0.001$). These results indicate that the constructed multifunctional FA-PFNB-SIRPα siRNA + US can effectively re-regulate the immunosuppressed TME and enhance the immunotherapeutic effect of the tumor by increasing the proportion of CTL, M1-like TAMs, and activating T cells, and decreasing the proportion of Tregs and M2-like TAMs.

Tumor mRNA analysis and verification of immune effect in vitro

To investigate the immune mechanism underlying the anti-tumor effect of FA-PFNB-SIRPα siRNA + US treatment, gene sequencing was conducted on tumor tissues obtained from both the PBS and the FA-PFNB-SIRPα siRNA + US groups following the completion of the treatment. A total of 54,160 transcripts were detected, among which 805 genes exhibited differential expression between the two groups, including 524 upregulated and 281 down-regulated genes (Fig. 8A). Through gene ontology (GO) and Kyoto Encyclopedia of Genes and Genomes (KEGG) enrichment analysis (Fig. 8B and C), it was discovered that the differentially expressed genes were primarily enriched in signaling pathways associated with immune response, antigen presentation and processing, cytokine interaction, inflammatory response, and T cell activation. Furthermore, a detailed analysis was performed on immune-related genes, revealing that genes involved

(See figure on next page.)

Fig. 6 Antitumor activity of FA-PFNB-SIRPα siRNA + ultrasound (US) in the NSCLC model. **A** Illustration of the in vivo experimental design. **B** NSCLC tumor growth curves in different groups (n = 5). **C** Spaghetti plots of NSCLC tumor growth in different groups (n = 5). **D** The body weight of mice in different groups(n = 5). **E** Tumor inhibition ratio in different groups(n = 5). **F** Image of representative NSCLC tumors in different groups. **G** Survival rate in different groups (n = 5). **H** and **I** TUNEL analysis of NSCLC tumors in different groups (Scale bar: 10μm). **J** H&E staining analysis of NSCLC tumors in different groups (Scale bar: 10μm). Data was presented by the mean ± SD. *$P < 0.05$; **$P < 0.01$; ***$P < 0.001$; ****$P < 0.0001$
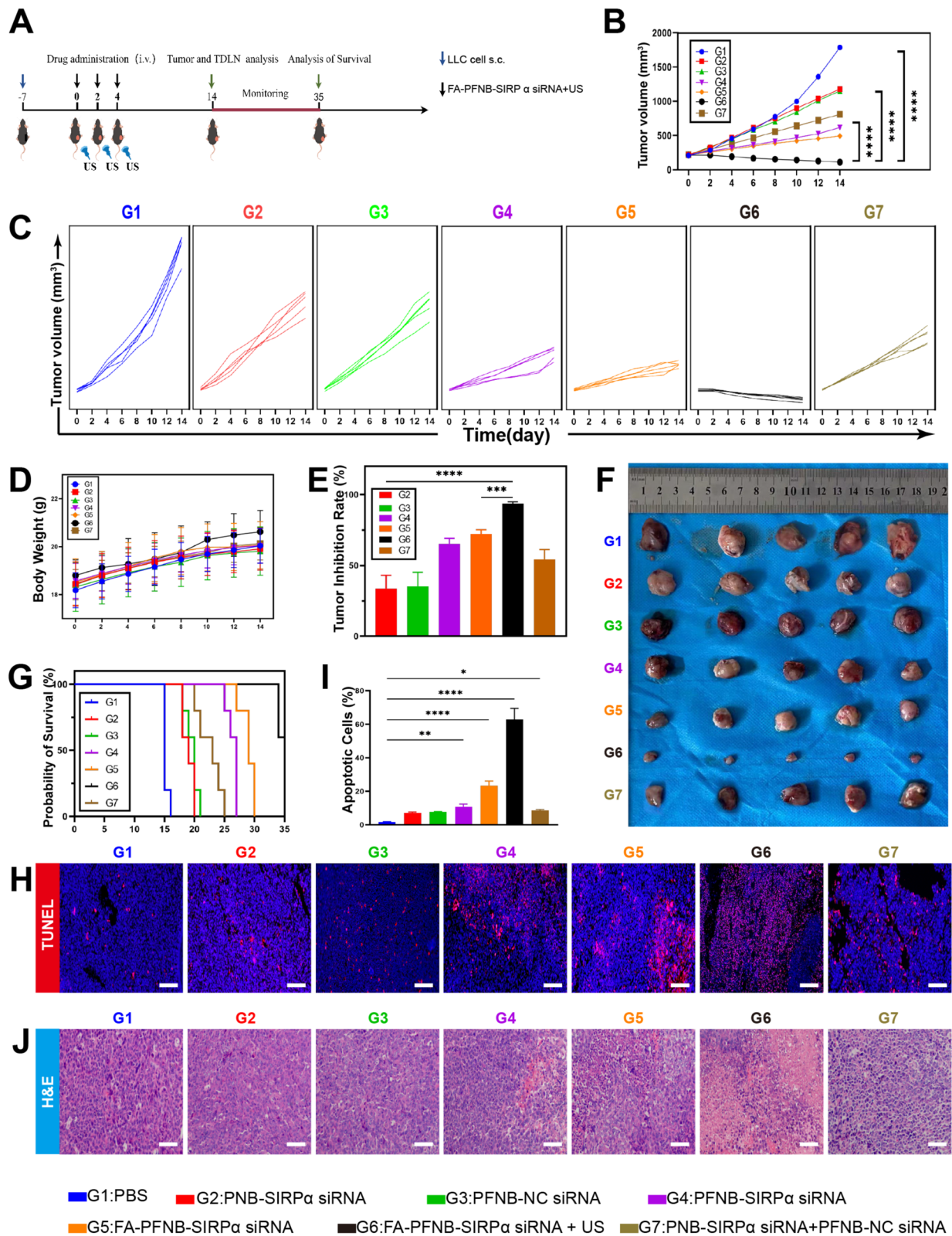
Fig. 6 (See legend on previous page.)

Li *et al. Journal of Nanobiotechnology*   (2024) 22:605
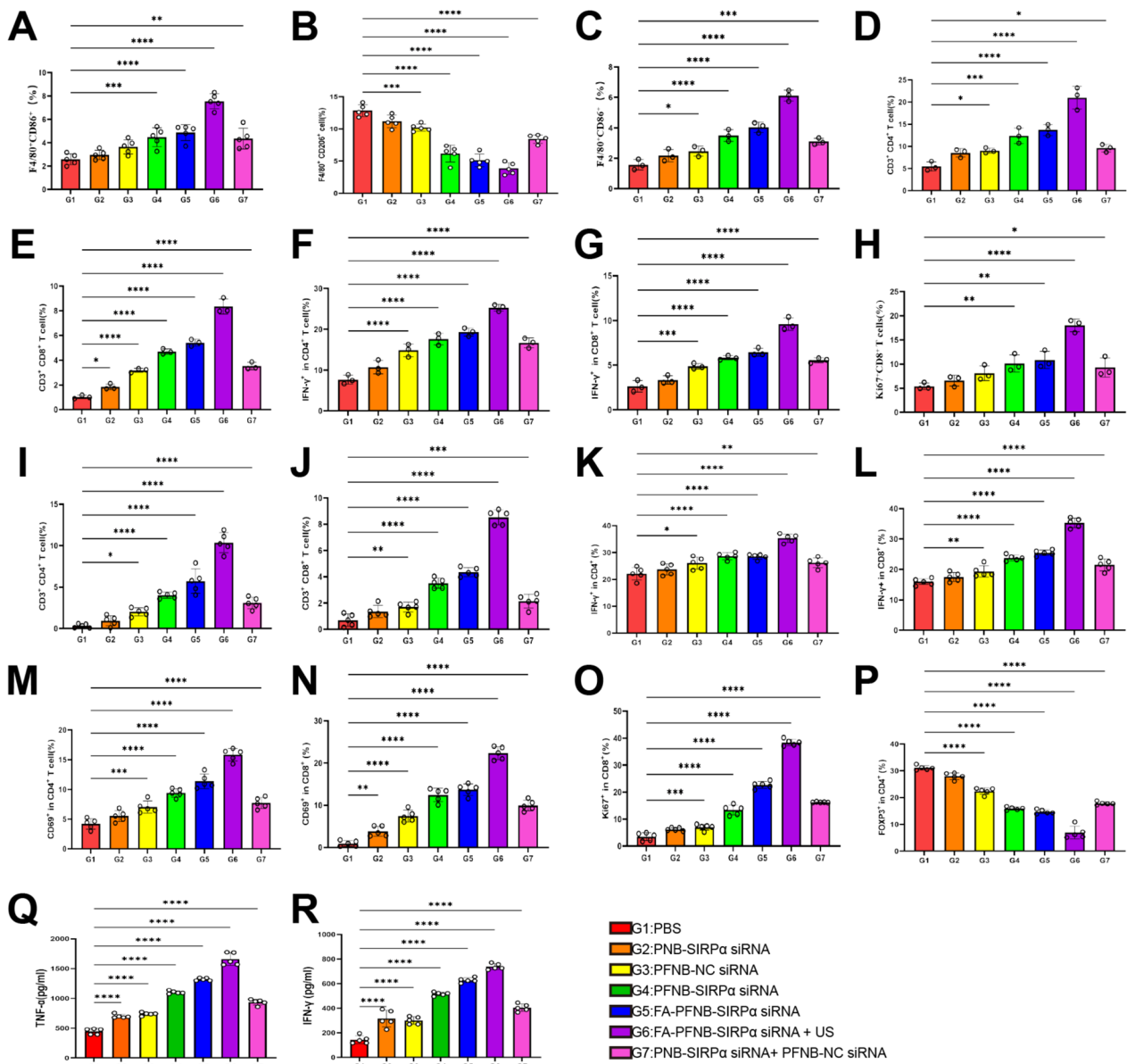
Page 18 of 26

Fig. 7 Anticancer immune response in the tumor and TDLNs. **A**, **B** M1-like macrophages (F4/80$^+$ CD86$^+$), M2-like macrophages (F4/80$^+$CD206$^+$) in tumor tissue(n = 5). **C** M1-like macrophages (F4/80$^+$ CD86$^+$) in TDLN (n = 3). **D**, **E** CD3$^+$CD4$^+$ and CD3$^+$CD8$^+$ T cells in TDLN (n = 3). **F**, **G** Activated CD4 $^+$and CD8$^+$ lymphocytes in TDLN (CD4$^+$IFNγ$^+$, CD8$^+$IFNγ$^+$) (n = 3). **H** Percentages of proliferation in CD8 lymphocytes in TDLN (CD8$^+$ki67$^+$) (n = 3). **I**, **J** CD3$^+$CD4$^+$and CD3$^+$CD8$^+$ T cells in tumor tissue(n = 5). **K**–**N** Activated CD4 and CD8 lymphocytes in tumors tissue (CD4$^+$IFNγ$^+$, CD4$^+$CD69$^+$.CD8$^+$IFNγ$^+$, CD8$^+$CD69$^+$) (n = 5). **O** Percentages of proliferation in CD8 lymphocytes in tumor tissue (CD8$^+$ki67$^+$) (n = 5). **P** Percentages of Tregs (CD4$^+$FOXP3$^+$) in tumor tissue (n = 5). **Q**, **R** ELISA analysis of IFN-γ and TNF-α in tumor tissue(n = 5). Data was presented by the mean ± SD. *P < 0.05; **P < 0.01; ***P < 0.001; ****P < 0.0001

in M1 macrophages, NK cell activation (Fig. 8D), antigen presentation and processing (Fig. 8E), and T cell maturation (Fig. 8F) were significantly upregulated in the FA-PFNB-SIRPαsiRNA + US treatment group. Figure 8G demonstrates the close relationships among these upregulated genes, which collectively contribute to innate and adaptive immunity. By elucidating these

immune-related gene alterations, this study sheds light on the potential mechanisms by which FA-PFNB-SIRPα + US treatment exerts its anti-tumor effects, particularly through the modulation of immune responses involving M1 macrophages, NK cells, antigen presentation, and T cell activation. They are closely related to functional networks (Fig. 8H), and involved in innate
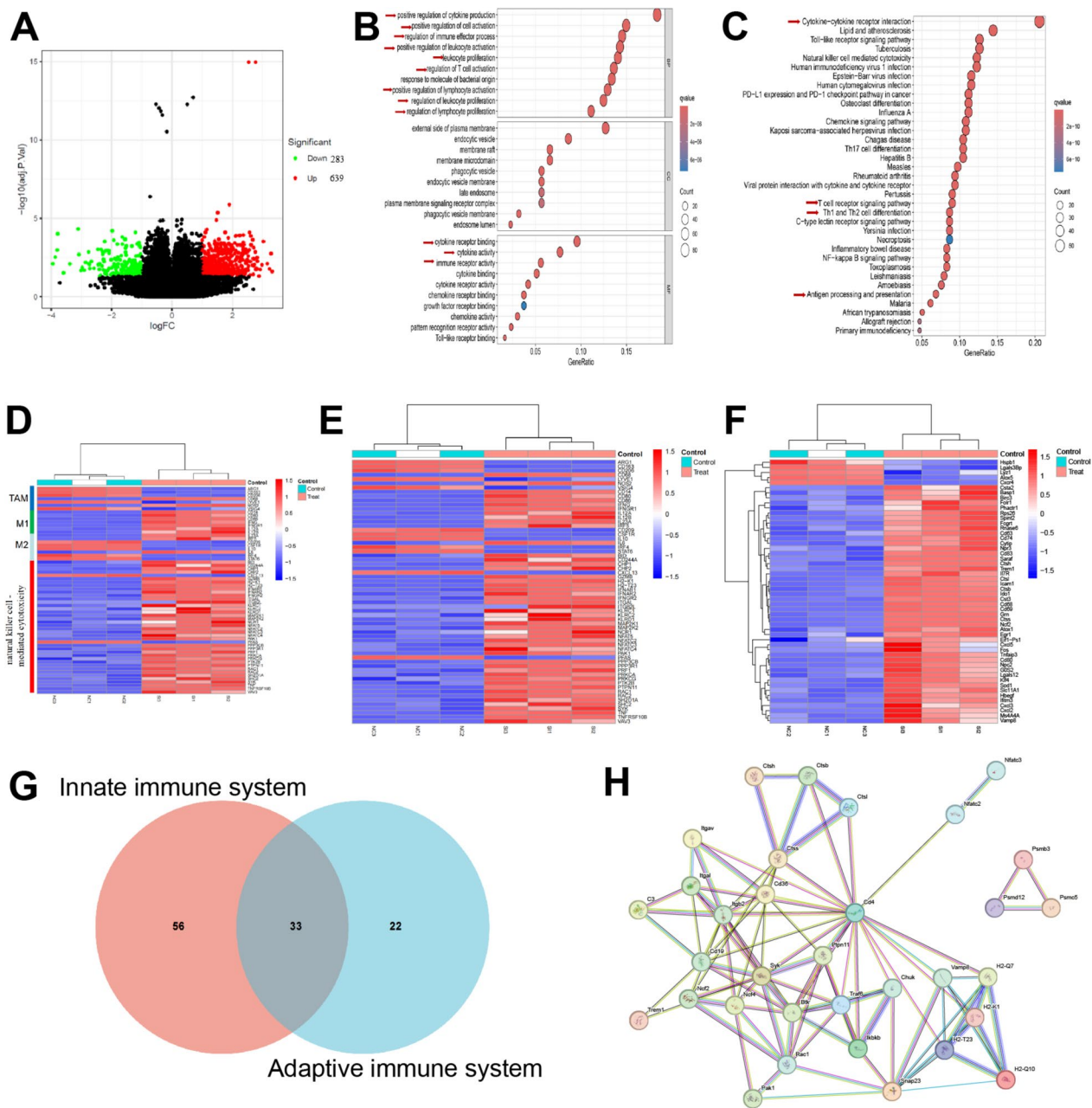
Fig. 8 Transcriptomic analysis. **A** A volcano plot of the FA-PFNB-SIRP α siRNA + US and PBS group. **B**, **C** Gene ontology annotation analysis (**B**) and Kyoto Encyclopedia of Genes and Genomes pathway analysis (**C**) in the FA-PFNB-SIRP α siRNA + US group. **D** Heat map illustrating differential gene expression of macrophages (M1 and M2) and natural killer cell-mediated cytotoxicity. **E**, **F** Heat map depicting differential expression of antigen processing and presentation-related genes (**E**) and T cell functional markers (**F**). **G** Venn diagram illustrating differentially expressed genes positively regulating both innate and adaptive immune responses. **H** Functional networks of differentially expressed immune-related genes regulating both innate and adaptive immune responses

and cellular immunity. In summary, FA-PFNB-SIRPα siRNA + US treatment can effectively activate the immune microenvironment and reverse the immunosuppressive state in NSCLC mice, thereby improving cancer immunotherapy.

Finally, the activation of specific immunity by FA-PFNB-SIRPα siRNA + US was further confirmed in vitro. The experiments were divided into three groups: M0 + LLC, M2 + LLC, and M2 + LLC + FA-PFNB-SIRPα siRNA + US, which were co-cultured for 24 h (LLC:

Li *et al. Journal of Nanobiotechnology*   (2024) 22:605

Page 20 of 26

TAMs = 4:1). Primary lymphocytes were isolated from the spleen of healthy mice (Fig. 9A). Subsequently, PBMCs were added in different groups at a ratio of 1:4:1(PBMC: LLC: TAMs). The co-culture system was treated for 24 h. The results showed that co-culture systems treated with FA-PFNB-SIRPα siRNA + US significantly increased the proportion of CD4 and CD8

positive T cells and significantly promoted the activation of CD8 positive T cells. The percentage of $CD69^+$ in $CD8^+$ and $ki67^+$ in $CD8^+$ positive cells increased (Fig. 9B–E and H–K). However, the proportion of $Foxp3^+$ in $CD4^+$ positive cells was significantly decreased (Fig. 9F, L). Meanwhile, the final treated supernatant was added to the medium containing LLC cells, which significantly
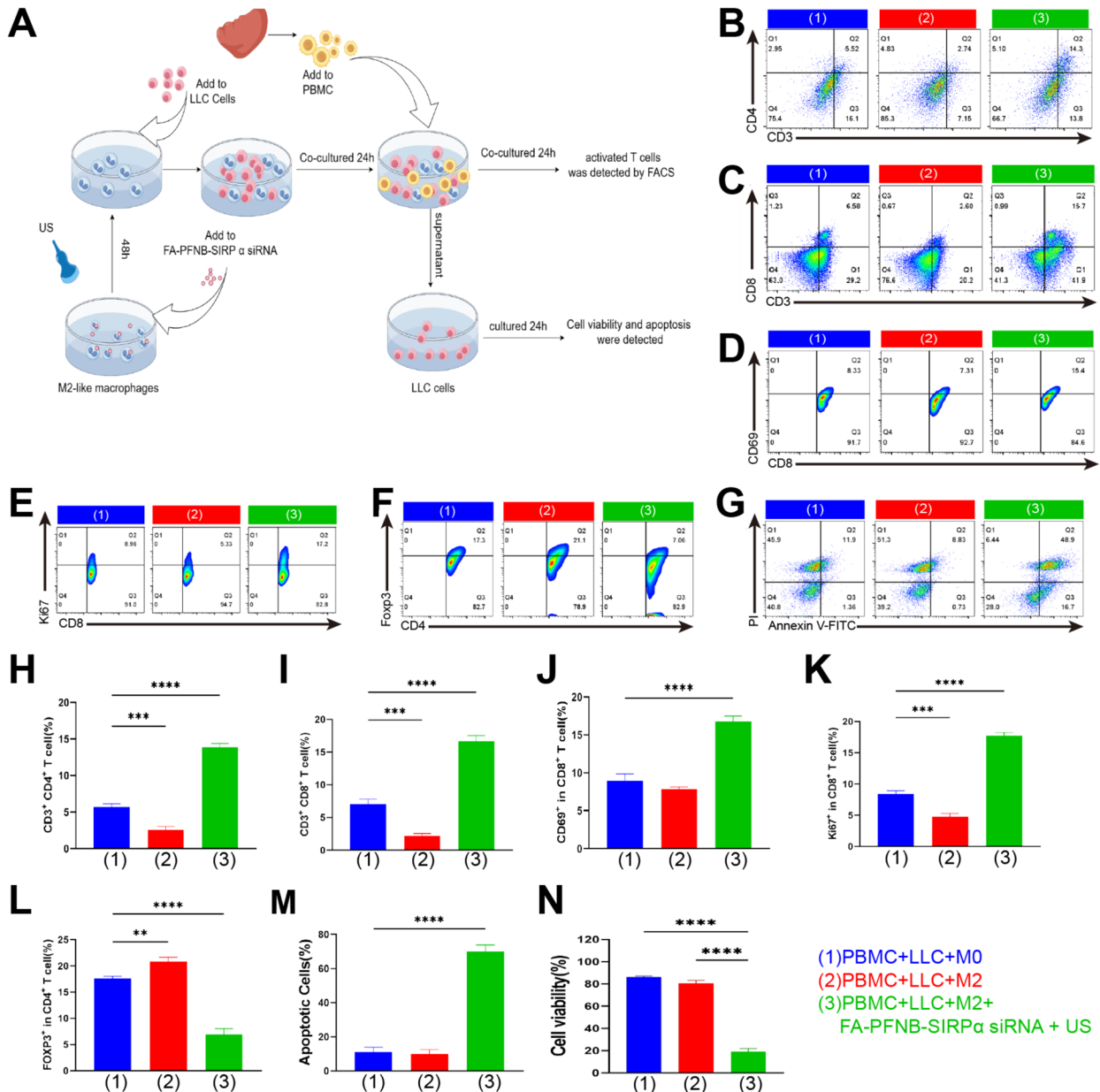
Fig. 9 In vitro immune activation validation and its anti-tumor effect. **A** Schematic diagram of a cell experiment. **B**, **C**, **H**, **I** The percentages of $CD3^+CD4^+$ T cells and $CD3^+CD8^+$ T cells(n = 3). **D**, **J** Activated CD8 lymphocytes ($CD8^+CD69^+$) (n = 3). **E**, **K** Percentages of proliferation in CD8 lymphocytes ($CD8^+ki67^+$) (n = 3). **F**, **L** Percentages of Tregs ($CD4^+FOXP3^+$) (n = 3). **G**, **M** Apoptosis assay of LLC cells under different conditioned media(n = 3). **N** CKK-8 method for measuring LLC cell viability under different culture media conditions(n = 3). Data was presented by the mean ± SD. *$P < 0.05$; **$P < 0.01$; ***$P < 0.001$; ****$P < 0.0001$

inhibited the viability of LLC and promoted the apoptosis of LLC cells (Fig. 9G, M, N). Overall, these results indicate that FA-PFNB-SIRPα siRNA + US effectively remodels M2-like TAMs and enhances the antigen presentation capacity of macrophages, which activates and promotes the secretion of proinflammatory T cells, killing tumor cells.

The biological safety evaluation of tumor therapy

To evaluate the biosafety of the experimental groups, we examined major organs (heart, liver, spleen, lung, and kidney) from tumor-bearing mice at the endpoint of the different treatments using staining techniques (Figure S30). No significant organ damage was observed after the treatments, resembling the findings in the PBS group. Additionally, when considering the recorded weight changes, as shown in Fig. 6D, it is evident that the materials utilized in this study are biocompatible and do not induce significant adverse effects in mice.

The results of the blood, liver function, and kidney function tests in each group were comparable to those of the PBS group, encompassing white blood cells (WBCs), red blood cells (RBCs), hemoglobin (HGB), alanine aminotransferase (ALT), aspartate aminotransferase (AST), total bilirubin (TBIL), creatinine (CREA), and Urea (UREA). These findings further support the biosafety profile of FA-PFNB-SIRPα siRNA + US treatment (Figure S31, 32).

Discussion

The successful infiltration and activation of immune cells in tumor tissues are essential for effective tumor immunotherapy [59]. TAMs, functioning as specialized antigen-presenting cells (APCs), play a crucial role in preventing the malignant transformation of cells in the innate immune response [60]. However, TAMs primarily exhibit immunosuppressive M2-like phenotypes, promoting various cancers' progression and metastasis [61]. Additionally, the overexpression of CD47 on tumor cells interacts with SIRP-α on the surface of macrophages, activating the "don't eat me" signaling pathway. This weakens the phagocytosis of macrophages on tumor cells, reduces antigen presentation ability, and inhibits the activation of downstream T cells, thus promoting tumor immune escape [62]. Therefore, targeting TAMs holds promise as an immunotherapy for NSCLC treatment.

Currently, several anti-TAM drugs are being evaluated in clinical trials, utilizing three main strategies [6]:(i) inhibition of TAM recruitment [63], (ii) depletion of TAMs [64], and (iii) remodeling of M2-like TAMs [65]. However, previous studies have indicated that inhibiting TAM recruitment and survival may not produce a durable anti-tumor response [8]; instead, reeducation strategies represent a more practical option as they improve immunosuppressive function and enhance antigen presentation. Magnetic nanoparticles (MNPs) have been extensively developed and broadly utilized in various biomedical applications, including magnetic resonance imaging, targeted drug delivery, gene therapy, magnetic separation of cells or biomolecules, in vivo cell tracking, tissue engineering, and hyperthermia for cancer therapy [66, 67]. Iron oxide MNPs, particularly superparamagnetic iron oxide nanoparticles, demonstrate significant potential across multiple domains within these nanoscience initiatives [68, 69]. Iron oxide are prevalently employed in biomedical applications due to their exceptional properties, including cost-effectiveness [70]. Studies have shown that iron oxide (Fe_3O_4) nanoparticles can effectively promote the transformation of M2-like TAMs into M1-like by activating the IRF5 pathway. In line with these findings, our experiment confirmed that Fe_3O_4 nanoparticles significantly increased the expression of IRF5 and CD86 in M2-like macrophages while significantly decreasing CD206 expression. This indicates the effectiveness of Fe_3O_4 nanoparticles in remodeling M2 macrophages. However, our study further revealed that re-educating M2-like macrophages using Fe_3O_4 nanoparticles alone was insufficient, and high doses of nano-Fe_3O_4 could affect macrophage viability. This may be attributed to the limited delivery efficiency of nanomedicine and the single-drug mechanism of action. Previous studies have demonstrated that blocking the CD47/SIRP-α axis enhances the phagocytosis of TAMs and dendritic cells, thereby activating the innate immune response, directly killing tumor cells, and enhancing antigen presentation, ultimately activating cytotoxic T cells and expanding the anti-tumor effect [71].

Recently, RNAi-based therapies have significantly advanced gene therapy [18]. Current studies indicate that targeting SIRPα can produce better immunotherapeutic effects than solely targeting CD47 on tumor cells [72]. Therefore, in this study, we employed SIRPα siRNA to knock down the SIRPα receptor on macrophage surfaces. Free siRNA has the disadvantages of low cellular uptake rate and susceptibility to nuclease degradation. Therefore, an RNAi technology-based immunotherapy delivery system with high transfection efficiency and effective macrophage targeting is essential for NSCLC tumors. While viral and non-viral vectors have been utilized in gene therapy delivery systems, viral vectors are constrained by potential oncogenicity, immunogenicity, and restricted loading capacity [73, 74]. Thus, we synthesized non-viral phase-transforming liposomal nanobubbles to deliver SIRPα siRNA and Fe_3O_4 nanoparticles. Under the action of LIFU, phase-transition NBs are transformed

Li *et al. Journal of Nanobiotechnology*   (2024) 22:605

Page 22 of 26

into microbubbles, followed by UTMD, resulting in the release of Fe_3O_4 nanoparticles. The sonoporation and cavitation effects can effectively increase tumor tissue and blood vessel permeability, promoting drug release into the extravascular space and enhancing cell nano-composite uptake [75]. Combining our findings, which showed significantly higher FRβ expression in M2-like macrophages than endothelial cells, we used FRβ as a target to enhance tumor-specific plasmid uptake [76]. Modified with FA the nanobubbles actively target M2-like macrophages, and ultrasound-induced sonoporation and cavitation effects are used in tandem to promote the delivery of SIRPα siRNA and Fe_3O_4 nanoparticles to M2-like macrophages. Our study showed that the US significantly improved SIRPα siRNA transfection in M2-like macrophages. Furthermore, combining FA modification with ultrasound irradiation led to a significantly higher SIRPα siRNA transfection efficiency than commercial Lipofectamine RNAiMAX Reagent, FA-PFNB, and PFNB delivery systems. Moreover, this approach promoted NB accumulation in vivo, as confirmed by multimodal imaging. It also significantly reduced SIRPα expression in macrophages in both in vivo and in vitro settings. Therefore, the US, combined with targeted NBs, holds important clinical application potentials in improving siRNA/drug targeting delivery.

In this study, combining the US with FA-PFNB-SIRPα siRNA significantly inhibited NSCLC tumor growth and substantially extended overall survival in mice. The remarkable anti-tumor efficacy of this treatment approach may be attributed to boosted anti-tumor immunity. For example, it can promote the polarization and phagocytosis of M1-like macrophages, suppress M2-like macrophage polarization, enhance the activation and proliferation of intertumoral cytotoxic T cells, and decrease Treg infiltration. Increasing intertumoral M1-like macrophages and enhancing antigen-presenting capacity required for naive T priming and T-cell-mediated anti-tumor immunity can be an effective anti-tumor strategy [8]. Our results demonstrated that US combined with FA-PFNB-SIRPα siRNA treatment significantly increased F4/80CD86 expression in macrophages, indicating a significant increase in M1 macrophages, in vitro and in vivo. Additionally, the US combined with FA-PFNB-SIRPα siRNA treatment significantly promoted the phagocytosis of F4/80$^+$ macrophages on LLC tumor cells. Further in vitro experiments revealed that the US combined with FA-PFNB-SIRPα siRNA treatment significantly promoted the proliferation and activation of lymphocytes and activated the immune microenvironment, leading to tumor cell killing. This may be linked to the polarization of M1-like macrophages and enhanced antigen presentation ability. Analysis of intertumoral

lymphocyte subsets and tumor tissue gene sequencing indicated that the US combined with FA-PFNB-SIRPα siRNA treatment significantly promoted the expression of M1 macrophage and antigen presentation-related genes in the tumor, activating innate and adaptive immunity. This was manifested by increased CD4 and CD8 positive T cells and their proliferation and activation. Additionally, the tumor infiltration by immuno-suppressive Treg cells was significantly reduced after FA-PFNB-SIRPα siRNA + US treatment. The significant increase in tumor apoptosis observed in mice treated with FA-PFNB-SIRPα siRNA + US resulted from the significantly enhanced anti-tumor immune response mediated by Fe_3O_4 nanoparticles and SIRPα siRNA delivery and in vitro experiments with PBMCs further confirmed these findings. Moreover, we found that FA-PFNB-SIRPα siRNA + US significantly increased M1 expression in tumor-draining lymph nodes and activated cytotoxic T cells. Furthermore, we discovered that the holistic delivery of nanomedicine was more effective and contributed to more synergistic activation of the immune response compared to separate injections of the two drugs simultaneously. Furthermore, FA-PFNB-SIRPα siRNA + US-mediated tumor-targeted delivery was well-tolerated in mice without causing systemic toxicity.

The strategy employed in this study offers several advantages over current immunotherapies. Macrophages, traditionally refractory cells [77], were targeted in this study. Ultrasound combined with FA-modified nanobubbles significantly improved the transfection efficiency of M2-like macrophages and promoted drug and gene enrichment in vivo, a challenge faced by previous gene delivery systems. Additionally, real-time multimodal imaging achieved through ultrasound combined with FA-modified NBs allows the detection of drug density and quantity in target organs. This study went beyond single-strategy M2 targeting to demonstrate the effectiveness and superiority of multi-modality combination therapy. Moreover, our targeted delivery system outperforms other tumor-targeting gene delivery systems reported in the literature. For example, commonly used cationic lipids in gene delivery systems are associated with high toxicity, limited efficiency, and non-specific delivery [78–80]. Conversely, our tumor-targeted gene delivery system is safe, easy to prepare, exhibits low immunogenicity and systemic toxicity, and combining ultrasound with FA modification further increases transfection efficiency.

Despite the extensive research conducted in this field, the limited penetration of ultrasound through lung tissue has bottlenecked studies on ultrasound-responsive drugs for treating lung diseases, particularly lung cancer. This limitation has also curtailed their clinical application. However, our clinical observations indicate a significant

diagnostic and therapeutic benefit of ultrasound in treating peripheral lung cancer. Consequently, this research holds substantial potential for managing inoperable peripheral NSCLC and as an adjunctive to immunotherapy for peripheral NSCLC. Moreover, the findings could guide immunotherapy strategies for other cancers exhibiting CD47 overexpression. Looking ahead, we are optimistic about technological advancements enabling the development of devices to enhance ultrasound penetration in lung tissues. Such progress would broaden the applicability of ultrasound-responsive drugs in treating lung diseases, underlining the transformative potential of our study in clinical settings.

Conclusions

The novel FA-modified NBs in this study exhibited high efficiency and safety in delivering Fe_3O_4 nanoparticles and SIRPα siRNA. This delivery system can effectively transform M2-like macrophages into M1, enhance their phagocytic capacity, promote antigen presentation, and subsequently induce T-cell activation while inhibiting the infiltration of immunosuppressive cells in NSCLC, which plays a crucial role in inhibiting the invasion and migration of cells. The US, in combination with a targeted NB system, is safe and well-tolerated in mice and is free from systemic toxicity, rendering it a dependable gene delivery system. With its potential for future applications, this strategy for NSCLC and potentially other tumor types offers a novel approach to cancer immunotherapy based on immune cell recruitment and activation, distinguishing it from current immunotherapies.

Abbreviations

NSCLC	Non-small cell lung cancer
TME	Tumor microenvironment
TAMs	Tumor-associated macrophages
IRF5	Interferon-regulatory factor 5
SIRPα	Signal regulatory protein α
RNAi	RNA interference
NPs	Nanoparticles
FA	Folic acid
FR	Folate receptor
US	Ultrasound
LIFU	Low-intensity focused ultrasound
PFP	Perfluoropentane
ADV	Acoustic droplet vaporization
DSPE-PEG2000-FA	FA-1,2-distearoyl-sn-glycero-3-phosphoethanolamine-N-[amino (polyethylene glycol)2000]
DOTAP	1,2-Dioleoacyl-3-trimethylammonium-propane
NBs	Nanobubbles
$CHCl_3$	Trichloromethane
DAPI	4′,6-Diamidino-2-phenylindole
PBS	Phosphate-buffered saline
FBS	Fetal bovine serum
DMEM	Dulbecco's modified Eagle's Medium
CFSE	Carboxyfluorescein succinimidyl ester
IL-4	Interleukin-4
DLS	Dynamic light scattering
TEM	Transmission electron microscope
NBs	Nanobubbles
CEUS	Contrast-enhanced ultrasound
LLC	Lewis's lung cancer
CCK-8	Cell Counting Kit-8
IFN-γ	Interferon-γ
TNF-α	Tumor necrosis factor-α
IL-10	Interleukin-10
ROI	Region of Interest
CTLs	Cytotoxic T lymphocytes
Tregs	Regulatory T cells
ELISA	Enzyme-linked immunosorbent assay
TDLNs	Tumor-draining lymph nodes
PBMC	Primary murine spleen-derived lymphocytes
H&E	Hematoxylin and eosin
ANOVA	One-way analysis of variance
PDI	Polydispersity index
MUVEC	Mouse umbilical vein endothelial cells
PA	Photoacoustic
MFI	Mean fluorescence intensity
UTMD	Ultrasound-mediated microbubble destruction
GO	Gene Ontology
KEGG	Kyoto Encyclopedia of Genes and Genomes
WBC	White blood cell
RBC	Red blood cell
HGB	Hemoglobin
ALB	Albumin
ALT	Alanine aminotransferase
AST	Aspartate aminotransferase
TBIL	Total bilirubin
CREA	Creatinine
UREA	Urea
APCs	Antigen-presenting cells
MNPs	Magnetic nanoparticles

Supplementary Information

The online version contains supplementary material available at https://doi.org/10.1186/s12951-024-02883-w.

Additional file 1.

Availability of data and materials

No datasets were generated or analysed during the current study.

Declarations

Ethics approval and consent to participate

All the animal experiments were performed with the approval of the Ethics Committee of Lanzhou University Second Hospital and all procedures were

Li *et al. Journal of Nanobiotechnology*   (2024) 22:605

Page 24 of 26

performed according to the guidelines and animal welfare protocols. The animal biomedical research authorization number is D2022-226.

Consent for publication
All authors declare that consent the publication of this study.

Competing interests
The authors declare no competing interests.

Author details
¹Ultrasound Medical Center, Gansu Province Clinical Research Center forā Ultrasonography, Gansu Province Medical Engineering Research Center for Intelligence Ultrasound, Lanzhou University Second Hospital, Lanzhou 730000, China. ²State Key Laboratory of Ultrasound in Medicine and Engineering, Institute of Ultrasound Imaging, The Second Affiliated Hospital, Chongqing Medical University, Chongqing 400010, People's Republic of China. ³Peking University Third Hospital, Beijing 100191, China. ⁴Department of Urology, Peking University First Hospital, Beijing, China.

References
1. Chen P, Liu Y, Wen Y, Zhou C. Non-small cell lung cancer in China. Cancer Commun (Lond). 2022;42:937–70.
2. Wang M, Herbst RS, Boshoff C. Toward personalized treatment approaches for non-small-cell lung cancer. Nat Med. 2021;27:1345–56.
3. Ettinger DS, Wood DE, Aisner DL, Akerley W, Bauman JR, Bharat A, Bruno DS, Chang JY, Chirieac LR, DeCamp M, et al. NCCN guidelines(R) insights: non-small cell lung cancer, version 2.2023. J Natl Compr Canc Netw. 2023;21:340–50.
4. Sun L, Bleiberg B, Hwang WT, Marmarelis ME, Langer CJ, Singh A, Cohen RB, Mamtani R, Aggarwal C. Association between duration of immunotherapy and overall survival in advanced non-small cell lung cancer. JAMA Oncol. 2023;9:1075–82.
5. Vesely MD, Zhang T, Chen L. Resistance mechanisms to anti-PD cancer immunotherapy. Annu Rev Immunol. 2022;40:45–74.
6. Pittet MJ, Michielin O, Migliorini D. Clinical relevance of tumour-associated macrophages. Nat Rev Clin Oncol. 2022;19:402–21.
7. Larroquette M, Guegan JP, Besse B, Cousin S, Brunet M, Le Moulec S, Le Loarer F, Rey C, Soria JC, Barlesi F, et al. Spatial transcriptomics of macrophage infiltration in non-small cell lung cancer reveals determinants of sensitivity and resistance to anti-PD1/PD-L1 antibodies. J Immunother Cancer. 2022;10.
8. Rodell CB, Arlauckas SP, Cuccarese MF, Garris CS, Li R, Ahmed MS, Kohler RH, Pittet MJ, Weissleder R. TLR7/8-agonist-loaded nanoparticles promote the polarization of tumour-associated macrophages to enhance cancer immunotherapy. Nat Biomed Eng. 2018;2:578–88.
9. Jiang Q, Wang K, Zhang X, Ouyang B, Liu H, Pang Z, Yang W. Platelet membrane-camouflaged magnetic nanoparticles for ferroptosis-enhanced cancer immunotherapy. Small. 2020;16: e2001704.
10. Gu Z, Liu T, Tang J, Yang Y, Song H, Tuong ZK, Fu J, Yu C. Mechanism of iron oxide-induced macrophage activation: the impact of composition and the underlying signaling pathway. J Am Chem Soc. 2019;141:6122–6.
11. Yu GT, Rao L, Wu H, Yang LL, Bu LL, Deng WW, Wu L, Nan XL, Zhang WF, Zhao XZ, et al. Myeloid-derived suppressor cell membrane-coated magnetic nanoparticles for cancer theranostics by inducing macrophage polarization and synergizing immunogenic cell death. Adv Funct Mater. 2018;28.
12. Jiang Z, Sun H, Yu J, Tian W, Song Y. Targeting CD47 for cancer immunotherapy. J Hematol Oncol. 2021;14:180.
13. Logtenberg MEW, Scheeren FA, Schumacher TN. The CD47-SIRPalpha immune checkpoint. Immunity. 2020;52:742–52.
14. Su Z, Dong S, Chen Y, Huang T, Qin B, Yang Q, Jiang X, Zou C. Microfluidics-enabled nanovesicle delivers CD47/PD-L1 antibodies to enhance antitumor immunity and reduce immunotoxicity in lung adenocarcinoma. Adv Sci (Weinh). 2023;10: e2206213.
15. Guo Y, Bao Q, Hu P, Shi J. Nanomedicine-based co-delivery of a calcium channel inhibitor and a small molecule targeting CD47 for lung cancer immunotherapy. Nat Commun. 2023;14:7306.
16. Tang Z, Zhong MC, Qian J, Galindo CC, Davidson D, Li J, Zhao Y, Hui E, Veillette A. CD47 masks pro-phagocytic ligands in cis on tumor cells to suppress antitumor immunity. Nat Immunol. 2023;24:2032–41.
17. Won Lee J, Kyu Shim M, Kim H, Jang H, Lee Y, Hwa Kim S. RNAi therapies: expanding applications for extrahepatic diseases and overcoming delivery challenges. Adv Drug Deliv Rev. 2023;201: 115073.
18. Yoon J, Shin M, Lee JY, Lee SN, Choi JH, Choi JW. RNA interference (RNAi)-based plasmonic nanomaterials for cancer diagnosis and therapy. J Control Release. 2022;342:228–40.
19. Zong Y, Lin Y, Wei T, Cheng Q. Lipid nanoparticle (LNP) enables mRNA delivery for cancer therapy. Adv Mater. 2023;35: e2303261.
20. Mishra VK, Rodriguez-Lecompte JC, Ahmed M. Nanoparticles mediated folic acid enrichment. Food Chem. 2024;456: 139964.
21. Cresswell GM, Wang B, Kischuk EM, Broman MM, Alfar RA, Vickman RE, Dimitrov DS, Kularatne SA, Sundaram CP, Singhal S, et al. Folate receptor beta designates immunosuppressive tumor-associated myeloid cells that can be reprogrammed with folate-targeted drugs. Cancer Res. 2021;81:671–84.
22. Sun X, Guo L, Shang M, Shi D, Liang P, Jing X, Meng D, Liu X, Zhou X, Zhao Y, Li J. Ultrasound mediated destruction of LMW-HA-loaded and folate-conjugated nanobubble for TAM targeting and reeducation. Int J Nanomedicine. 2020;15:1967–81.
23. Xu D, Pan C, Liu S, Guo J, Zheng P, Zhang M. Efficient alleviation granular sludge floatation in a high-rate anammox reactor by dosing folate. Water Res. 2024;264: 122249.
24. Movendane Y, Sipalo MG, Chan LCZ. Advances in folic acid biosensors and their significance in maternal, perinatal, and paediatric preventive medicine. Biosensors (Basel). 2023;13.
25. Nie W, Yu T, Liu X, Wang B, Li T, Wu Y, Zhou X, Ma L, Lin Y, Qian Z, Gao X. Non-viral vector mediated CKb11 with folic acid modification regulates macrophage polarization and DC maturation to elicit immune response against cancer. Bioact Mater. 2021;6:3678–91.
26. Tie Y, Zheng H, He Z, Yang J, Shao B, Liu L, Luo M, Yuan X, Liu Y, Zhang X, et al. Targeting folate receptor beta positive tumor-associated macrophages in lung cancer with a folate-modified liposomal complex. Signal Transduct Target Ther. 2020;5:6.
27. Liang J, Qiao X, Qiu L, Xu H, Xiang N, Ding H, Chen Y. Engineering versatile nanomedicines for ultrasonic tumor immunotherapy. Adv Sci (Weinh). 2024;11: e2305392.
28. Kim H, Choi Y, Kim SY, Pahk KJ. Increased intracellular diffusivity of macromolecules within a mammalian cell by low-intensity pulsed ultrasound. Ultrason Sonochem. 2023;100: 106644.
29. Hou J, Zhou J, Chang M, Bao G, Xu J, Ye M, Zhong Y, Liu S, Wang J, Zhang W, et al. LIFU-responsive nanomedicine enables acoustic droplet vaporization-induced apoptosis of macrophages for stabilizing vulnerable atherosclerotic plaques. Bioact Mater. 2022;16:120–33.
30. Um W, Ko H, You DG, Lim S, Kwak G, Shim MK, Yang S, Lee J, Song Y, Kim K, Park JH. Necroptosis-inducible polymeric nanobubbles for enhanced cancer sonoimmunotherapy. Adv Mater. 2020;32: e1907953.
31. Xie Z, Wang J, Luo Y, Qiao B, Jiang W, Zhu L, Ran H, Wang Z, Zhu W, Ren J, Zhou Z. Tumor-penetrating nanoplatform with ultrasound "unlocking" for cascade synergistic therapy and visual feedback under hypoxia. J Nanobiotechnology. 2023;21:30.
32. Jeong M, Lee Y, Park J, Jung H, Lee H. Lipid nanoparticles (LNPs) for in vivo RNA delivery and their breakthrough technology for future applications. Adv Drug Deliv Rev. 2023;200: 114990.
33. Nie W, He Y, Mi X, He S, Chen J, Zhang Y, Wang B, Zheng S, Qian Z, Gao X. Immunostimulatory CKb11 gene combined with immune checkpoint PD-1/PD-L1 blockade activates immune response and simultaneously overcomes the immunosuppression of cancer. Bioact Mater. 2024;39:239–54.
34. Han S, Wang W, Wang S, Yang T, Zhang G, Wang D, Ju R, Lu Y, Wang H, Wang L. Tumor microenvironment remodeling and tumor therapy based on M2-like tumor associated macrophage-targeting nano-complexes. Theranostics. 2021;11:2892–916.
35. Manzini G, Barcellona ML, Avitabile M, Quadrifoglio F. Interaction of diamidino-2-phenylindole (DAPI) with natural and synthetic nucleic acids. Nucleic Acids Res. 1983;11:8861–76.

36. Chen Y, Shu X, Guo JY, Xiang Y, Liang SY, Lai JM, Zhou JY, Liu LH, Wang P. Nanodrugs mediate TAMs-related arginine metabolism interference to boost photodynamic immunotherapy. J Control Release. 2024;367:248–64.

37. Taylor SC, Nadeau K, Abbasi M, Lachance C, Nguyen M, Fenrich J. The ultimate qPCR experiment: producing publication quality, reproducible data the first time. Trends Biotechnol. 2019;37:761–74.

38. Kaluderovic MR, Mojic M, Gómez-Ruiz S, Mijatovic S, Maksimovic-Ivanic D. Anticancer activity of organogallium(III) complexes in colon cancer cells. Anticancer Agents Med Chem. 2016;16:359–64.

39. Lee S, Ho JY, Liu JJ, Lee H, Park JY, Baik M, Ko M, Lee SU, Choi YJ, Hur SY. CKD-602, a topoisomerase I inhibitor, induces apoptosis and cell-cycle arrest and inhibits invasion in cervical cancer. Mol Med. 2019;25:23.

40. Yu-Ju WuC, Chen CH, Lin CY, Feng LY, Lin YC, Wei KC, Huang CY, Fang JY, Chen PY. CCL5 of glioma-associated microglia/macrophages regulates glioma migration and invasion via calcium-dependent matrix metalloproteinase 2. Neuro Oncol. 2020;22:253–66.

41. Wang K, Jiang X, Jiang Y, Liu J, Du Y, Zhang Z, Li Y, Zhao X, Li J, Zhang R. EZH2-H3K27me3-mediated silencing of mir-139-5p inhibits cellular senescence in hepatocellular carcinoma by activating TOP2A. J Exp Clin Cancer Res. 2023;42:320.

42. Refaat A, Yap ML, Pietersz G, Walsh APG, Zeller J, Del Rosal B, Wang X, Peter K. In vivo fluorescence imaging: success in preclinical imaging paves the way for clinical applications. J Nanobiotechnology. 2022;20:450.

43. John S, Hester S, Basij M, Paul A, Xavierselvan M, Mehrmohammadi M, Mallidi S. Niche preclinical and clinical applications of photoacoustic imaging with endogenous contrast. Photoacoustics. 2023;32: 100533.

44. Li M, Bian X, Chen X, Fan N, Zou H, Bao Y, Zhou Y. Multifunctional liposome for photoacoustic/ultrasound imaging-guided chemo/photothermal retinoblastoma therapy. Drug Deliv. 2022;29:519–33.

45. Yang K, Han W, Jiang X, Piffko A, Bugno J, Han C, Li S, Liang H, Xu Z, Zheng W, et al. Zinc cyclic di-AMP nanoparticles target and suppress tumours via endothelial STING activation and tumour-associated macrophage reinvigoration. Nat Nanotechnol. 2022;17:1322–31.

46. Chen Y, Du M, Yuan Z, Chen Z, Yan F. Spatiotemporal control of engineered bacteria to express interferon-gamma by focused ultrasound for tumor immunotherapy. Nat Commun. 2022;13:4468.

47. Kan Y, Song M, Cui X, Yang Q, Zang Y, Li Q, Li Y, Cai W, Chen Y, Weng X, et al. Muyin extract inhibits non-small-cell lung cancer growth by inducing autophagy and apoptosis in vitro and in vivo. Phytomedicine. 2022;96: 153834.

48. van't Veer LJ. Bernards R: Enabling personalized cancer medicine through analysis of gene-expression patterns. Nature. 2008;452:564–70.

49. Li TF, Li K, Zhang Q, Wang C, Yue Y, Chen Z, Yuan SJ, Liu X, Wen Y, Han M, et al. Dendritic cell-mediated delivery of doxorubicin-polyglycerol-nanodiamond composites elicits enhanced anti-cancer immune response in glioblastoma. Biomaterials. 2018;181:35–52.

50. Wang G, Jiang Y, Xu J, Shen J, Lin T, Chen J, Fei W, Qin Y, Zhou Z, Shen Y, Huang P. Unraveling the plasma protein corona by ultrasonic cavitation augments active-transporting of liposome in solid tumor. Adv Mater. 2023;35: e2207271.

51. Xu M, Qi Y, Liu G, Song Y, Jiang X, Du B. Size-dependent in vivo transport of nanoparticles: implications for delivery, targeting, and clearance. ACS Nano. 2023;17:20825–49.

52. Karshafian R, Bevan PD, Williams R, Samac S, Burns PN. Sonoporation by ultrasound-activated microbubble contrast agents: effect of acoustic exposure parameters on cell membrane permeability and cell viability. Ultrasound Med Biol. 2009;35:847–60.

53. Locati M, Curtale G, Mantovani A. Diversity, mechanisms, and significance of macrophage plasticity. Annu Rev Pathol. 2020;15:123–47.

54. Pan L, Wang B, Chen M, Ma Y, Cui B, Chen Z, Song Y, Hu L, Jiang Z. Lack of SIRP-alpha reduces lung cancer growth in mice by promoting anti-tumour ability of macrophages and neutrophils. Cell Prolif. 2023;56: e13361.

55. Lv WH, Xu C, Wu H, Zhu YY, Akakuru OU, Du H, Nie F, Wu AG, Li J. Ultrasound-visualized nanocarriers with siRNA for targeted inhibition of M2-like TAM polarization to enhance photothermal therapy in NSCLC. Nano Res. 2023;16:882–93.

56. Zhou B, Mo Z, Lai G, Chen X, Li R, Wu R, Zhu J, Zheng F. Targeting tumor exosomal circular RNA cSERPINE2 suppresses breast cancer progression by modulating MALT1-NF-. J Exp Clin Cancer Res. 2023;42:48.

57. Matic J, Deeg J, Scheffold A, Goldstein I, Spatz JP. Fine tuning and efficient T cell activation with stimulatory aCD3 nanoarrays. Nano Lett. 2013;13:5090–7.

58. Moldoveanu D, Ramsay L, Lajoie M, Anderson-Trocme L, Lingrand M, Berry D, Perus LJM, Wei Y, Moraes C, Alkallas R, et al. Spatially mapping the immune landscape of melanoma using imaging mass cytometry. Sci Immunol. 2022;7:eabi5072.

59. Lahiri A, Maji A, Potdar PD, Singh N, Parikh P, Bisht B, Mukherjee A, Paul MK. Lung cancer immunotherapy: progress, pitfalls, and promises. Mol Cancer. 2023;22:40.

60. Zhang X, Li S, Malik I, Do MH, Ji L, Chou C, Shi W, Capistrano KJ, Zhang J, Hsu TW, et al. Reprogramming tumour-associated macrophages to outcompete cancer cells. Nature. 2023;619:616–23.

61. Kloosterman DJ, Akkari L. Macrophages at the interface of the co-evolving cancer ecosystem. Cell. 2023;186:1627–51.

62. van Duijn A, Van der Burg SH, Scheeren FA. CD47/SIRPalpha axis: bridging innate and adaptive immunity. J Immunother Cancer. 2022;10.

63. Nywening TM, Wang-Gillam A, Sanford DE, Belt BA, Panni RZ, Cusworth BM, Toriola AT, Nieman RK, Worley LA, Yano M, et al. Targeting tumour-associated macrophages with CCR2 inhibition in combination with FOLFIRINOX in patients with borderline resectable and locally advanced pancreatic cancer: a single-centre, open-label, dose-finding, non-randomised, phase 1b trial. Lancet Oncol. 2016;17:651–62.

64. Gomez-Roca CA, Italiano A, Le Tourneau C, Cassier PA, Toulmonde M, D'Angelo SP, Campone M, Weber KL, Loirat D, Cannarile MA, et al. Phase I study of emactuzumab single agent or in combination with paclitaxel in patients with advanced/metastatic solid tumors reveals depletion of immunosuppressive M2-like macrophages. Ann Oncol. 2019;30:1381–92.

65. Sun L, Kees T, Almeida AS, Liu B, He XY, Ng D, Han X, Spector DL, McNeish IA, Gimotty P, et al. Activating a collaborative innate-adaptive immune response to control metastasis. Cancer Cell. 2021;39(1361–1374): e1369.

66. Liang X, Chen M, Bhattarai P, Hameed S, Tang Y, Dai Z. Complementing cancer photodynamic therapy with ferroptosis through iron oxide loaded porphyrin-grafted lipid nanoparticles. ACS Nano. 2021;15:20164–80.

67. Zhang HC, Deng L, Liu HQ, Mai SY, Cheng ZL, Shi GZ, Zeng H, Wu Z. Enhanced fluorescence/magnetic resonance dual imaging and gene therapy of liver cancer using cationized amylose nanoprobe. Mater Today Bio. 2022;13.

68. Kohzadi S, Najmoddin N, Baharifar H, Shabani M. Functionalized SPION immobilized on graphene-oxide: anticancer and antiviral study. Diam Relat Mater. 2022;127.

69. Long MM, Li Y, He HL, Gu N. The story of ferumoxytol: synthesis production, current clinical applications, and therapeutic potential. Adv Healthc Mater. 2024;13.

70. Wang SR, Hou YL. New types of magnetic nanoparticles for stimuli-responsive theranostic nanoplatforms. Adv Sci. 2024;11.

71. Veillette A, Chen J. SIRPalpha-CD47 immune checkpoint blockade in anticancer therapy. Trends Immunol. 2018;39:173–84.

72. Huang C, Wang X, Wang Y, Feng Y, Wang X, Chen S, Yan P, Liao J, Zhang Q, Mao C, et al. Sirpalpha on tumor-associated myeloid cells restrains anti-tumor immunity in colorectal cancer independent of its interaction with CD47. Nat Cancer. 2024;5(3):500–516.

73. Baum C, Kustikova O, Modlich U, Li Z, Fehse B. Mutagenesis and oncogenesis by chromosomal insertion of gene transfer vectors. Hum Gene Ther. 2006;17:253–63.

74. Bessis N, GarciaCozar FJ, Boissier MC. Immune responses to gene therapy vectors: influence on vector function and effector mechanisms. Gene Ther. 2004;11(Suppl 1):S10-17.

75. Xing L, Shi Q, Zheng K, Shen M, Ma J, Li F, Liu Y, Lin L, Tu W, Duan Y, Du L. Ultrasound-mediated microbubble destruction (UMMD) facilitates the delivery of CA19-9 targeted and paclitaxel loaded mPEG-PLGA-PLL nanoparticles in pancreatic cancer. Theranostics. 2016;6:1573–87.

76. Puig-Kroger A, Sierra-Filardi E, Dominguez-Soto A, Samaniego R, Corcuera MT, Gomez-Aguado F, Ratnam M, Sanchez-Mateos P, Corbi AL. Folate receptor beta is expressed by tumor-associated macrophages and constitutes a marker for M2 anti-inflammatory/regulatory macrophages. Cancer Res. 2009;69:9395–403.

77. Zhang Y, Wang Y, Zhang C, Wang J, Pan D, Liu J, Feng F. Targeted gene delivery to macrophages by biodegradable star-shaped polymers. ACS Appl Mater Interfaces. 2016;8:3719–24.

Li *et al. Journal of Nanobiotechnology*   (2024) 22:605

Page 26 of 26

78. Yin H, Kanasty RL, Eltoukhy AA, Vegas AJ, Dorkin JR, Anderson DG. Non-viral vectors for gene-based therapy. Nat Rev Genet. 2014;15:541–55.
79. Kullberg M, McCarthy R, Anchordoquy TJ. Systemic tumor-specific gene delivery. J Control Release. 2013;172:730–6.
80. Mitchell MJ, Billingsley MM, Haley RM, Wechsler ME, Peppas NA, Langer R. Engineering precision nanoparticles for drug delivery. Nat Rev Drug Discov. 2021;20:101–24.

Publisher's Note